

Sensitivity of MPI-ESM Sea Level Projections to Its Ocean Spatial Resolution

CHATHURIKA WICKRAMAGE ^a, ARMIN KÖHL,^a JOHANN JUNGCLAUS,^b AND DETLEF STAMMER^a

^a Center for Earth System Research and Sustainability (CEN), Universität Hamburg, Hamburg, Germany

^b Max Planck Institute for Meteorology, Hamburg, Germany

(Manuscript received 2 June 2022, in final form 22 November 2022)

ABSTRACT: The dependence of future regional sea level changes on ocean model resolution is investigated based on Max Planck Institute Earth System Model (MPI-ESM) simulations with varying spatial resolution, ranging from low resolution (LR), high resolution (HR), to eddy-rich (ER) resolution. Each run was driven by the shared socioeconomic pathway (SSP) 5-8.5 (fossil-fueled development) forcing. For each run the dynamic sea level (DSL) changes are evaluated by comparing the time mean of the SSP5-8.5 climate change scenario for the years 2080–99 to the time mean of the historical simulation for the years 1995–2014. Respective results indicate that each run reproduces previously identified large-scale DSL change patterns. However, substantial sensitivity of the projected DSL changes can be found on a regional to local scale with respect to model resolution. In comparison to models with parameterized eddies (HR and LR), enhanced sea level changes are found in the North Atlantic subtropical region, the Kuroshio region, and the Arctic Ocean in the model version capturing mesoscale processes (ER). Smaller yet still significant sea level changes can be found in the Southern Ocean and the North Atlantic subpolar region. These sea level changes are associated with changes in the regional circulation. Our study suggests that low-resolution sea level projections should be interpreted with care in regions where major differences are revealed here, particularly in eddy active regions such as the Kuroshio, Antarctic Circumpolar Current, Gulf Stream, and East Australian Current.

SIGNIFICANCE STATEMENT: Sea level change is expected to be more realistic when mesoscale processes are explicitly resolved in climate models. However, century-long simulations with eddy-resolving models are computationally expensive. Therefore, current sea level projections are based on climate models in which ocean eddies are parameterized. The representation of sea level by these models considerably differs from actual observations, particularly in the eddy-rich regions such as the Southern Ocean and the western boundary currents, implying erroneous ocean circulation that affects the sea level projections. Taking this into account, we review the sea level change pattern in a climate model with featuring an eddy-rich ocean model and compare the results to state-of-the-art coarser-resolution versions of the same model. We found substantial DSL differences in the global ocean between the different resolutions. Relatively small-scale ocean eddies can hence have profound large-scale effects on the projected sea level which may affect our understanding of future sea level change as well as the planning of future investments to adapt to climate change around the world.

KEYWORDS: Ocean; Sea level; Climate models; Mesoscale models; Model comparison

1. Introduction

Rising sea levels are among the largest threats of anthropogenic global warming to society, with far-reaching consequences for many coastal and island populations around the globe (Church et al. 2011; Fox-Kemper et al. 2021). Our understanding of the global mean sea level trends has improved significantly over the past decades based on coordinated modeling efforts, such as the Coupled Model Intercomparison Project (CMIP) and the analysis of past observations (e.g., Church et al.

2011; Fox-Kemper et al. 2021). However, a quantitative understanding of processes that lead to regional to local-scale sea level changes is still pending, which affects the ability to accurately forecast future coastal changes (Church et al. 2013a). Although the quantitative budget of the global sea level rise is understood, insufficient data hampers the understanding on regional and coastal scale, which makes improving modeling efforts essential for closing the gaps.

Physically, regional to local-scale sea level change is a global problem as it depends on processes taking place locally as well as remotely. As such, it is directly or indirectly affected by all components of the climate system as well as contributions originating from the solid Earth such as vertical seafloor movement or changes in gravity (Stammer et al. 2013). However, the relative contribution of individual processes or forcing components to the regional or local sea level changes is strongly dependent on the spatial and temporal scales under consideration and might also change under global warming conditions.

In this context a caveat of previous CMIP projections is that underlying climate models are of relatively low spatial

 Denotes content that is immediately available upon publication as open access.

 Supplemental information related to this paper is available at the Journals Online website: <https://doi.org/10.1175/JCLI-D-22-0418.s1>.

Corresponding author: Chathurika Wickramage, chathurika.wickramage@uni-hamburg.de

DOI: 10.1175/JCLI-D-22-0418.1

© 2023 American Meteorological Society. For information regarding reuse of this content and general copyright information, consult the [AMS Copyright Policy](https://www.ametsoc.org/PUBSReuseLicenses) (www.ametsoc.org/PUBSReuseLicenses).

TABLE 1. Summary of MPI-ESM projections used in this study.

Configuration	MPI-ESM-LR	MPI-ESM-HR	MPI-ESM-ER
Atmospheric grid	T63	T127	T127
Atmospheric grid space at the equator (km)	210	104	104
Atmospheric grid space at 50°N (km)	129	67	67
Atmosphere nominal resolution (km)	200	100	100
Atmospheric vertical levels	47 (0.01 hPa top level)	95 (0.01 hPa top level)	95 (0.01 hPa top level)
Ocean grid	GR1.5	TP04	TP6M
Ocean grid spacing at equator (km)	185		
Ocean grid spacing near poles (km)	15	~30 (north), 20 to 10 (south)	~7 (north), 5 to 3 (south); 2 to 3 Weddell and Ross Seas)
Ocean nominal resolution (km)	150	40	10
Ocean vertical levels	40	40	40
Ocean-eddy resolving (Li and von Storch 2013)	No	No (eddy permitting)	Yes (eddy rich)

resolution, thereby intrinsically excluding the impact of resolved ocean eddies on the solution. To what extent existing sea level projections are thus biased toward large-scale climate mode responses as opposed to regional dynamical balances remains therefore to be understood, making it difficult to provide quantitative information about future sea level projections in specific regions, such as coastlines. This situation now gradually changes as climate projections from eddy-resolving models are becoming available accounting for the dynamical processes associated with boundary or coastal current dynamics, which are important for accurate small-scale sea level change information (e.g., van Westen et al. 2020; van Westen and Dijkstra 2021; Li et al. 2022). Given these new opportunities, it is now timely to test previous CMIP sea level change projections against novel eddy-rich climate projections.

Against this background, the aim of this paper is to provide an understanding of the sensitivity of CMIP type sea level projections to model resolution and, thus, to define an uncertainty level in CMIP previous projections resulting from the lack of small-scale processes and eddy mechanisms. Specifically, we aim to quantify differences in the resulting sea level projections obtained under shared socioeconomic pathway (SSP) 5-8.5 forcing (O'Neill et al. 2017) with respect to lower-resolution simulations using a hierarchy of spatial resolutions. The respective work will be based on the eddy-rich Max Planck Institute Earth System Model (MPI-ESM-ER) experiments (Gutjahr et al. 2019), which have been performed as part of the CMIP6-endorsed HighResMIP (Haarsma et al. 2016). At the same time, we aim to identify causes for those changes in terms of mechanisms, which can result from differences in the ocean dynamics and differences in the air–sea exchange of heat, freshwater, or momentum. Geographically, our work focuses on the North Atlantic, the North Pacific, and the Southern Ocean, where large-scale effects from meso-scale eddies can be expected, given the presence of strong and eddy-rich western boundary currents.

The structure of the remaining paper is as follows: Section 2 describes the model and the evaluation methods used. Common characteristics of sea level change in the models are described in detail in section 3. In section 4, we compare the ocean model

projection in each basin. We conclude and summarize with section 5.

2. Materials and methods

a. Climate model simulations with MPI-ESM

Our study is based on climate projections obtained with the MPI-ESM1.2 and performed under the protocol of the CMIP phase 6 (CMIP6; Eyring et al. 2016). The MPI-ESM is a fully coupled climate model, using ECHAM6 (Stevens et al. 2013) for the atmosphere and MPIOM (Jungclaus et al. 2013) for the ocean. Details on the CMIP6 version in comparison with its predecessor can be found in Mauritsen et al. (2019). Our study considers three versions of the same model configuration, including the low-resolution (LR), high-resolution (HR), and eddy-rich (ER) models, all driven by the SSP5-8.5 (fossil-fueled development) (O'Neill et al. 2017) forcing. From each model simulation monthly mean fields are available. Configurations for all experiments evaluated here are summarized in Table 1.

The coupled control simulations were initialized and forced following the CMIP6 protocol for HR and LR. The reference year for the preindustrial control simulation (piControl) is 1850, and it is conducted under conditions that have been selected to be typical of the time before the start of large-scale industrialization. A control simulation typically begins after an initial spinup phase, during which the climate system reaches a state close to an equilibrium (Eyring et al. 2016). For ER, the coupled control simulation was however initialized following the CMIP6-HighResMIP protocol (Haarsma et al. 2016). The ER control run was initialized after 30 years of spinup initialized from the averaged state of the Met Office Hadley Centre EN4 observational dataset from 1950 to 1954 (Good et al. 2013) for the ocean and ER atmosphere initialized from HR atmospheric state (Gutjahr et al. 2019). The length of control run is 1000 years for LR, 500 years for HR, and 200 years for ER.

The low-resolution version of MPI-ESM (MPI-ESM-LR) approximately has a 1.9° horizontal resolution for the atmosphere (spectral truncation at T63; 210 km at the equator; 192 × 96 longitude/latitude) and 47 hybrid sigma pressure level extending to a 0.01 hPa top level. The ocean component

has a bipolar 1.5° horizontal resolution (GR1.5; approximately 150 km near the equator; 256 × 220 longitude/latitude) and 40 vertical levels with layer thickness ranging from 12 m near the surface to several hundred meters at depth. The horizontal grid spacing varies from 185 km in the tropical Pacific to 22 km around Greenland. The poles of the ocean model are over Greenland and Antarctica (coast of the Weddell Sea). The LR version cannot capture mesoscale ocean processes and dynamics (for more details, [Mauritsen et al. 2019](#)).

The high-resolution configuration, MPI-ESM-HR ([Müller et al. 2018](#)), uses a 0.9° horizontal resolution (T127; 384 × 192 longitude/latitude) for the atmosphere, which is approximately 100 km around the equator. HR has a relatively highly resolved stratosphere extending to a 0.01 hPa top level with 95 vertical levels (L95). A tripolar grid 0.4° horizontal resolution (TP04; 802 × 404 longitude/latitude) is used for the ocean component. Two poles are placed in the Northern Hemisphere over central Asia (Siberia) and Canada, providing quasi-homogeneous resolution of a approximately 40 km in the Arctic Ocean. In the Southern Hemisphere, grid distances decrease with increasing latitude. South of the Antarctic Circumpolar Current (ACC) at around 60°S the resolution is 20 km. HR comprises 40 unevenly spaced vertical levels, allocating 20 levels within the upper 700 m. HR is permitting eddies in the tropics but not resolving the Rossby radius in the higher latitudes. Even though HR fails to resolve the Rossby radius length scales, key for the representation of boundary currents and fronts, it still can capture reasonable eddy-like structures (see [Jungclauss et al. 2013](#); [Müller et al. 2018](#)).

The Gent–McWilliams (GM) parameterization ([Gent and McWilliams 1990](#)) of mesoscale eddies is used in LR and HR. The GM coefficients in HR and LR are constant and quite small. They are scaled with the grid spacing. The GM parameterization decreases linearly with increasing resolution, and a value of 250 m^{−2} s^{−1} was chosen for a grid cell that is 400 km wide ([Gutjahr et al. 2019](#)).

The eddy-rich MPI-ESM-ER ([Gutjahr et al. 2019](#)) has the same T127/L95 atmospheric component as HR. However, the horizontal resolution of the ocean component is on a tripolar 6-min (TP6M) horizontal grid (approximately 0.1° or 10 km) in both latitude and longitude, and has 80 vertical levels. ER has three poles over North America, Russia, and Antarctica. In the eddy-rich-resolution model simulations, the GM parameterization for mesoscale eddies is disabled, and eddy effects are resolved according to the ratio of the first baroclinic deformation radius to the horizontal grid spacing. Eddies are not resolved at higher latitudes and over shallow/shelf regions. The grid resolution is smaller south of 50°S ([Table 1](#); for more details, check [Mauritsen et al. 2019](#); [Putrasahan et al. 2021](#)). The ER model has nominal horizontal resolution of ~10 km which means that the large-scale (order of 1000 km) and oceanic mesoscale eddies (order of 10 and larger) are resolved almost everywhere; however, the ocean submesoscale eddies are typically less than 10 km are not included in the ER simulation. In addition, the air–sea interactions from processes such as mesoscale storms are not resolved by the atmospheric component of ER model.

As part of our analysis, we compare results from all model version described above under the SSP5-8.5 climate forcing scenario

covering 2080–99, to their historical simulations during 1995–2014. In all cases we consider ensemble means using all available members, which are 10 members in LR, 2 in HR, and 3 in ER to minimize the impact of climate variability. Prior to analyzing the model output, we interpolated it onto the same grid of 1° horizontal resolution. As the development of ER was computationally expensive, it has not been tuned and spun up according to the standard of HR and LR ([Mauritsen et al. 2019](#)). Therefore, the linear trend obtained from the only member of the control run was removed from the historical and scenario data. While we focus mostly on effects of ocean resolution, we note that LR features also considerably lower resolution in the atmosphere. Therefore, we put particular emphasis in the discussion on changes we diagnose in the ER configuration, which was run with the same atmosphere as the HR model.

b. Analyzing model output

This study considers the dynamic sea level (DSL), which is defined as the mean sea level above the geoid due to ocean dynamics ([Gregory et al. 2019](#)):

$$\zeta = \eta - \eta'. \quad (1)$$

Here ζ is the variable “zos” according to the CMIP terminology ([Griffies et al. 2016](#)), η , which is named “sterodynamic sea level,” is the sea surface height relative to a reference geopotential surface, and η' denotes a global mean ([Gregory et al. 2019](#)). Hence, DSL change ($\Delta\zeta$) should have a zero global mean by definition. We therefore subtracted the global mean from each input field.

As we are interested in future sea level change, our work focuses on the dynamic sea level change ($\Delta\zeta$) pattern, which is calculated from the difference between the DSL change in SSP5-8.5 forcing scenario ($\Delta\eta_s$) relative to the DSL change in the historical simulation ($\Delta\eta_h$):

$$\Delta\zeta = \Delta\eta_s - \Delta\eta_h. \quad (2)$$

Considering that changes in circulation and changes in wind stress in principle are the key drivers of these changes, we also calculated changes in the barotropic streamfunction ψ , changes in surface wind stress, and variation in the meridional overturning circulation and analyzed their differences as function of model resolution.

The Sverdrup streamfunction was estimated using wind stress data based on the Sverdrup relation ([Sverdrup 1947](#)). The Sverdrup transport was integrated zonally along a latitude (y) from the eastern boundary (x_e) to each zonal location (x) of the basin as follows:

$$\psi_{sv} = \frac{1}{\beta\rho} \int_{x_e}^x \text{curl}(\tau) dx', \quad (3)$$

where β denotes the meridional derivative of the Coriolis parameter, ρ is the mean density of the ocean, and $\text{curl}(\tau)$ denotes the wind stress curl.

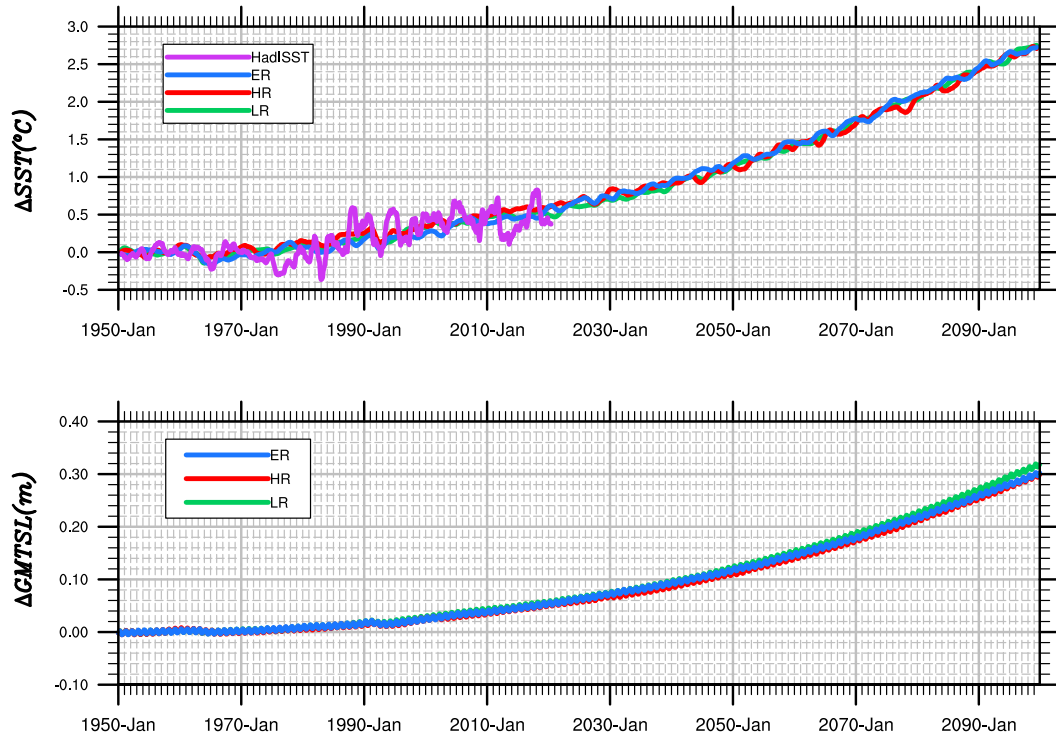


FIG. 1. Global 12-month running mean (a) sea surface temperature and (b) thermosteric sea level change for MPI-ESM-ER, MPI-ESM-HR, and MPI-ESM-LR, relative to the 1950s. The purple line in (a) represents a 12-month running mean of respective global mean HadISST values.

To analyze the meridional displacement of gyres, the mean latitude y of the barotropic streamfunction is calculated according to

$$\theta = \frac{\int \psi \times y \, dx \, dy}{\int \psi \, dx \, dy}. \quad (4)$$

We consider the zero contour as the boundary of each gyre and consider positive (negative) barotropic streamfunction values for subtropical (subpolar) gyre. The contours between the minimum and maximum transport (positive contours) in the Drake Passage were considered to calculate the mean central latitude of ACC transport.

c. Significance and trend

Assuming that the variance remains unchanged under climate forcing conditions, the 95% significance of the difference of changes between the resolutions ER and HR was determined according to the formula, $\sqrt{(2\sigma_{ER}^2/N_{ER} + 2\sigma_{HR}^2/N_{HR})} \times t_{95\%}$, with $t_{95\%}$ the Student t value, N_{ER} and N_{HR} are the respective numbers of members, and σ_{ER}^2 and σ_{HR}^2 are the variances of the ER and HR control simulations, respectively. The factor 2 accounts for the fact that the changes have twice the variance of the fields they are calculated from. A similar method was applied to calculate the error bar or envelope, $(1/\sqrt{N})\sqrt{2\sigma_{ER}^2} \times t_{95\%}$

for the ensemble mean changes [see von Storch and Zwiers (2002) for more details]. The linear least squares fitting was used to calculate the yearly average time series trend. The analyses were performed using CDO and NCL software (NCL 2019).

3. Commonalities of sea level changes in MPI-ESM

Over the past years, the global ocean has accounted for around 91% of anthropogenically induced Earth's heat content increase, resulting in an observed thermal expansion and associated sea level rise of about 0.54 (0.40–0.68) mm yr⁻¹ over the years from 1901 to 2018 (Fox-Kemper et al. 2021). In contrast, the simulated thermal expansion in IPCC AR6 leads to sea level rise of 30 (24–36) cm under SSP5-8.5 for the year 2100 relative to a baseline of 1995–2014. From the MPI-ESM model simulations we can infer a comparable global mean thermosteric sea level (GMTSL) rise (Fig. 1) of 30.30, 30.06, and 31.95 cm at the end of the twenty-first century relative to the 1950s for ER, HR, and LR, respectively. Over the period 1901–2018, changes are around 60 mm and compare well with the observed change of 63.2 mm due to thermal expansion (Fox-Kemper et al. 2021). The average simulated rate of thermosteric sea level rise due to global ocean heating for the SPP5-8.5 scenario is 3.31 mm yr⁻¹ in ER, 3.34 mm yr⁻¹ in HR, and 3.51 mm yr⁻¹ in LR between 2030 and 2099.

Figure 1 also compares the increase in thermosteric sea level rise with the respective increases in global SST. On global average, both curves suggest an equivalent increase in

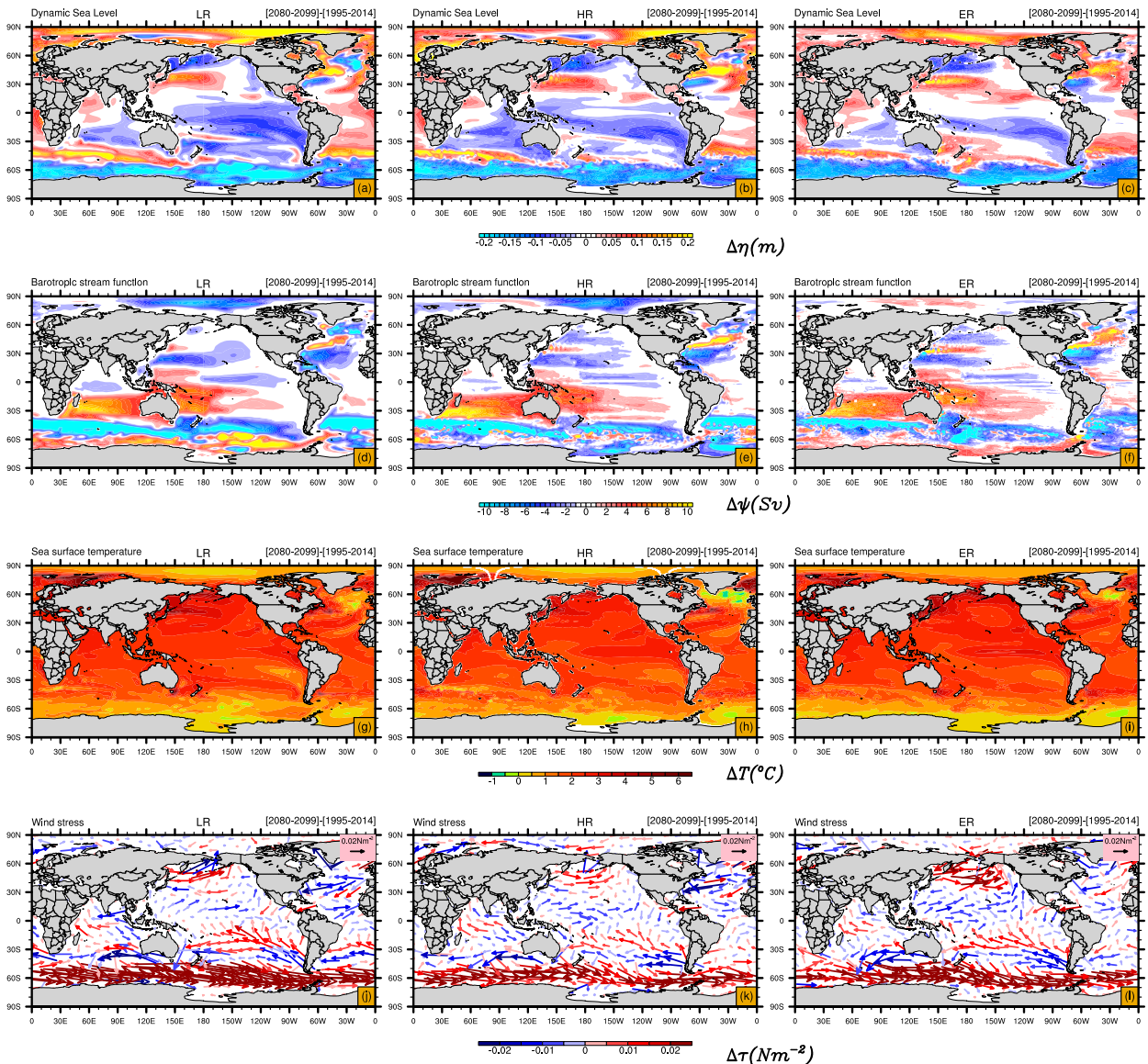


FIG. 2. Anomalies of (a)–(c) dynamic sea level (m), (d)–(f) barotropic streamfunction (Sv), (g)–(i) sea surface temperature ($^{\circ}\text{C}$), and (j)–(l) wind stress (N m^{-2}), for (left) MPI-ESM-LR, (center) MPI-ESM-HR, and (right) MPI-ESM-ER between the SSP5-8.5 averaged over the period 2080–99 and the historical period averaged over the years 1995–2014.

thermosteric sea level rise of $0.11 \text{ m per } 1^{\circ}\text{C}$ of SST increase. However, SST curves are considerable noisier and, in that sense, can only be considered a very crude proxy for thermosteric sea level rise. This holds especially for individual ensemble members and should be true also for the real world. We note that a respective correspondence cannot be expected to hold on regional scale due to the temperature dependence of the thermosteric expansion coefficient and the influence of salinity.

The common global pattern of LR, HR, and ER for the changes in DSL (in m), the barotropic streamfunction (BSF; Sv; $1 \text{ Sv} \equiv 10^6 \text{ m}^3 \text{ s}^{-1}$), and the wind stress (N m^{-2}) are discussed in this section. These changes between the patterns

over the SSP5-8.5 years 2080–99 relative to the historical simulation (years 1995–2014) are shown in Fig. 2. We will discuss how the models differ from one another on regional scale in the following section.

The DSL is a helpful tool for analyzing the ocean processes contributing to sea level changes due to the close link between the DSL and the ocean circulation through the geostrophic relation. According to Figs. 2a–c, sea level changes are not homogeneous in the global ocean but show diverse regional patterns. At the end of the century, the respective sea level change leads to a dipole pattern in the North Atlantic with generally increasing sea level north of the Gulf Stream (in the southern part of the subpolar gyre) and a decrease in the

subtropical gyre. An opposite dipole pattern exists in the North Pacific, where sea level is higher south of the Kuroshio (in the subtropical region) and lower farther to the north (in the subpolar region). In the Southern Ocean, the ridge-like pattern is associated with a sea level increase north of $\sim 50^{\circ}\text{S}$ and decrease south of $\sim 50^{\circ}\text{S}$. The aforementioned sea level change patterns have also been reported previously, such as Chen et al. (2019), Church et al. (2013a,b), Couldrey et al. (2021), Fox-Kemper et al. (2021), Gregory et al. (2016), and Lyu et al. (2020), and common to all the models. As in previous studies (Prandi et al. 2012; Rose et al. 2019; Xiao et al. 2020), the highest sea level rise is also found in our models in the Arctic Ocean.

Many changes in DSL displayed in Figs. 2a–c can be associated with changes in the vertically integrated large-scale circulation as depicted by BSF (Figs. 2d–f). In the North Atlantic, circulation in subpolar regions north of the Gulf Stream and Labrador Sea and the subtropical gyre weaken, whereas the circulation southeast of Greenland strengthens (negative BSF anomalies in high latitude). The latter is accompanied by a smaller DSL. However, the opposite happens in the North Pacific, where subpolar gyre and the Kuroshio region (northern part of subtropical gyre) strengthens, while the southern part of subtropical gyre weakens. A band of positive streamfunction north of Gulf Stream could possibly indicate the poleward shift of the North Atlantic Subtropical Gyre. Moreover, Southern Ocean circulation strengthens between 40° and 50°S in all models (Figs. 2d–f).

While almost every corner in the world is heating up, a cooling temperature patch, known as warming hole (aka cold blob), is identified in the vicinity of southeast Greenland (Figs. 2g–i). This warming hole feature, however, appears to be north of the warming hole stated in earlier studies in response to warming (e.g., Chemke et al. 2020; Drijfhout et al. 2012; Gervais et al. 2018; Menary and Wood 2018). Together with the warming hole, a patch of DSL decline (Figs. 2a–c), and a reinforced high latitude circulation (Figs. 2d–f) are identified in the same subpolar region in all configurations. Numerous previous studies have discussed the occurrence of the warming hole as a result of a weakening Atlantic meridional overturning circulation (AMOC) (such as Caesar et al. 2018; Drijfhout et al. 2012; Gervais et al. 2018; Keil et al. 2020; Menary and Wood 2018; Rahmstorf et al. 2015).

The variation in the BSF field is linked to the changes in the wind stress curl field by the Sverdrup relation. However, it might also reflect the changes in the interior density gradients and/or interactions with sloping bottom bathymetry (e.g., Yeager 2015). We examine the Sverdrup relation in the North Atlantic and North Pacific Oceans later in section 4. A distinct feature of wind stress changes in the models is the strengthening of the westerly wind in the Southern Ocean at the end of the twenty-first century (Figs. 2j–l). Over most of the Pacific Ocean except the tropical North Pacific wind stress strengthens. Changes over the Atlantic are less clear, leading mostly to weakened wind stress, except for the eastern subtropical North Atlantic.

4. Discrepancies of regional sea level change in MPI-ESM

In the following we will discuss the detailed resolution dependence of the time mean changes from historical to SSP5-8.5 on the model resolution separately for the North Atlantic, the North Pacific, and the Southern Ocean.

a. North Atlantic

DSL change in the subpolar gyre region is characterized by two distinct features: a decrease in the basins southeast of Greenland and an increase in the rest of the subpolar gyre (Figs. 3a–c). Statistically significant differences at 95% are marked by dots in the spatial pattern difference and by nonoverlapping error bars in the zonal averages. This DSL decrease over the basins southeast of Greenland (the Irminger Sea and Icelandic Basin) is smallest in ER and largest in LR (by the magnitude of ~ 0.2 m see in Figs. 3a,c,d,e). The increase in the Labrador Sea and farther south until north of the Gulf Stream is also smaller in ER than HR and LR (by the magnitude of ~ 0.16 m see in Figs. 3d,e). The changes southeast of Greenland dominate the zonal mean (north of 50°N) of DSL, indicating a prominent decrease in LR and almost no change in HR (Fig. 4a). In contrast, ER shows an overall sea level increase in the northern part of the subpolar gyre, pointing to a smaller decline in the basins southeast of Greenland (Figs. 3c,d, 4a). In the southern part of the subpolar gyre (between 40° and 50°N), the MPI-ESM models show a DSL increase with the largest rise in HR (Fig. 4a). The increase in HR can be noticed in the spatial pattern by a negative and positive sign of the difference north of the Gulf Stream (north of 40°N) in Figs. 3e and 3f, respectively.

These changes in sea level also reflect changes in circulation indicated by the vertically integrated flow (displayed in Figs. 6a–c). The cyclonic circulation in southeast of Greenland strengthens in LR and somewhat less so in HR. It is even lesser in ER (Figs. 6a–c), as does decline in sea level. Subpolar gyre circulation weakens in the Labrador Sea and the southern part of the gyre. In contrast, the weakening is considerably larger in the ER model. A weakening subpolar gyre as seen in ER was also reported for the circulation changes from the 1990s to the 2000s observed by altimetry data (Lee et al. 2010; Häkkinen and Rhines 2004, 2009), with inconclusive attribution to whether these changes remain part of natural climate variability or are already a sign of a long-term trend. Nevertheless, the circulation changes can have important consequences for the distribution of water masses as a weakening subpolar gyre can lead to an increasing transport of warm and salty Atlantic water into the Nordic seas during the historical period (Hátún et al. 2005) and significant reduction in Labrador Sea deep convection.

Many previous studies have also highlighted the relation between weakening AMOC and DSL changes in the North Atlantic (Bouttes et al. 2014; Chen et al. 2019; Fox-Kemper et al. 2021; Hu et al. 2011; Levermann et al. 2005; Lyu et al. 2020; Pardaens et al. 2011; Yin et al. 2009, 2010). The projected change of the AMOC is likely to depend on the model resolution and therefore impact DSL differently. The pattern of the AMOC change is nearly identical to its mean

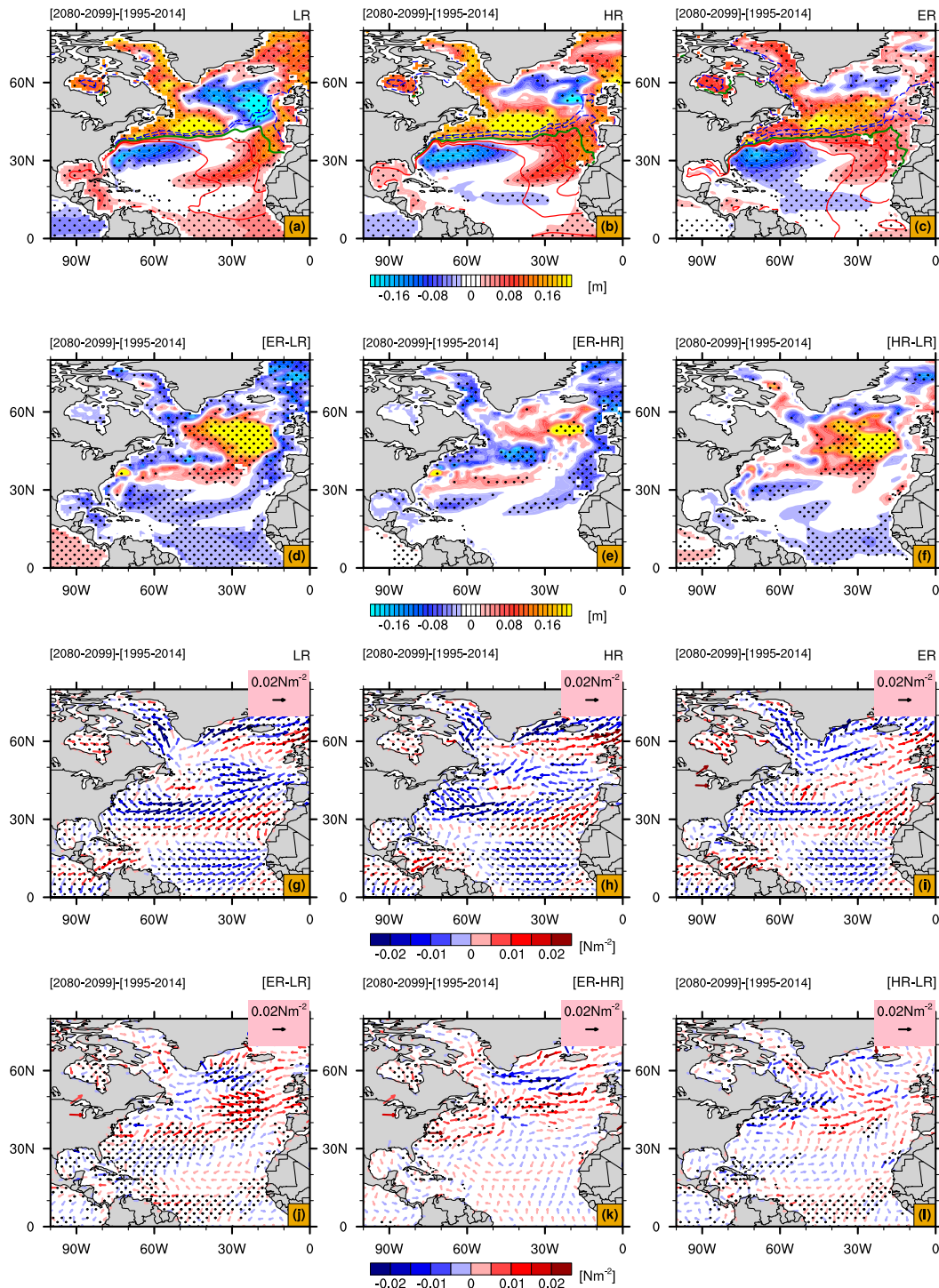


FIG. 3. North Atlantic differences of (a)–(f) dynamic sea level (m) and (g)–(l) wind stress (N m^{-2}); panels (a)–(c) and (g)–(i) illustrate the anomalies of the SSP5-8.5 (2080–99) average relative to the historical simulation, averaged over 1995–2014 for MPI-ESM-LR in (a) and (g), MPI-ESM-HR in (b) and (h), and MPI-ESM-ER in (c) and (i); panels (d)–(f) and (j)–(l) illustrate the differences of the anomalies between the models [ER minus LR in (d) and (j), ER minus HR in (e) and (k), and HR minus LR in (f) and (l)]. The contours represent the historical mean (1995–2014; contour interval is 0.1 m). The contour colors denote solid red for the positive values, green line for the zero contour, and dash blue for the negative values. In all panels stippling indicates statistically significant differences (95% confidence level). All projections were interpolated onto the same grid prior to computing differences of the anomalies.

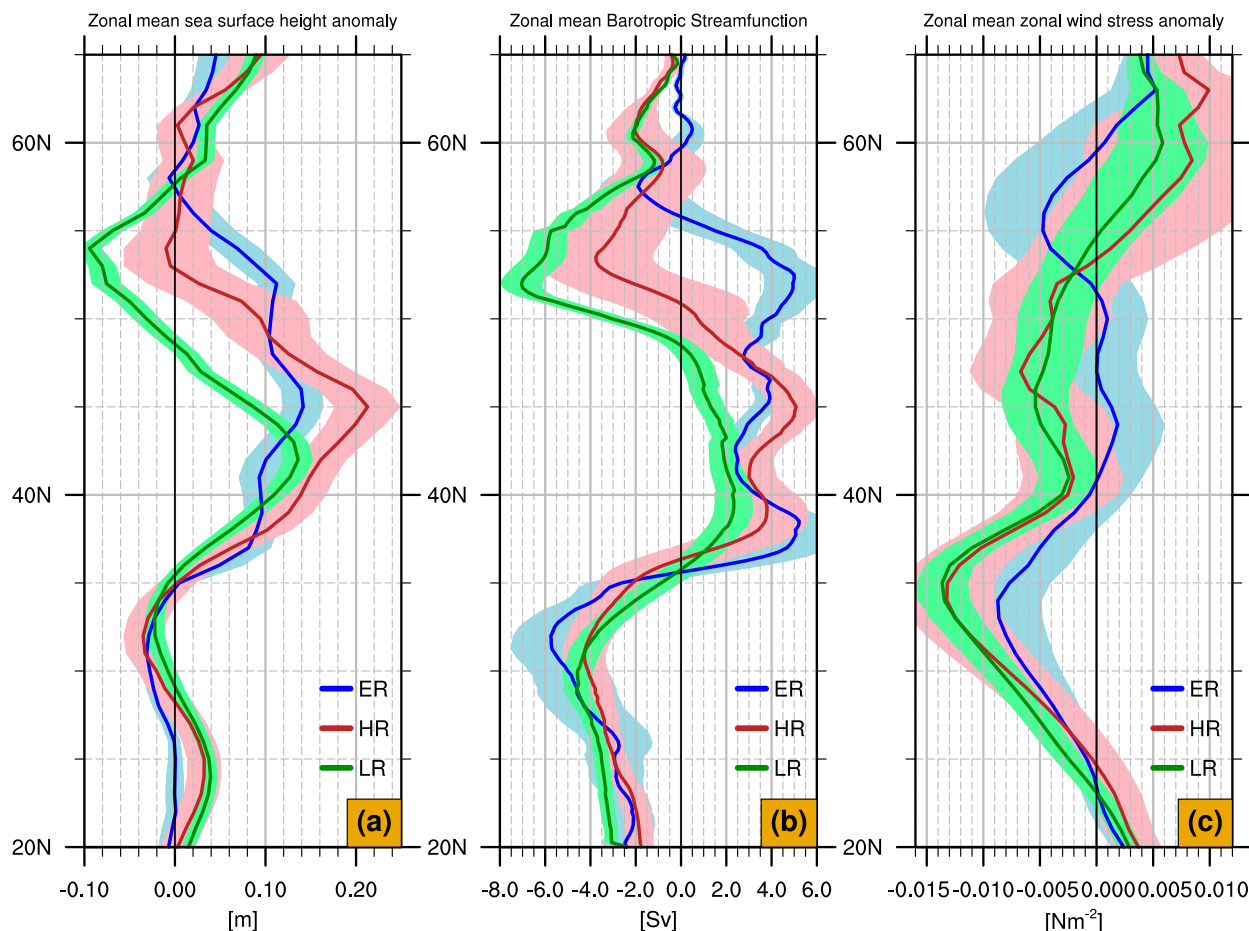


FIG. 4. North Atlantic (a) zonal mean sea surface height (m); (b) zonal mean barotropic streamfunction (Sv); (c) zonal mean zonal wind stress (N m^{-2}) anomalies, each for the time mean differences over historical simulation and SSP5-8.5 for ER, HR, and LR, respectively. Error bar envelopes represent two standard deviations.

AMOC (Figs. 5a–c), indicating a consistent weakening of all branches from historical to SSP5-8.5 by about one-third of its strength. The overlaid contours of historical mean in Figs. 5a–c provide a comparison with its anomalies. Similar to the DSL change, the warming hole feature becomes smaller in size with improved horizontal resolution, especially in ER compared to HR (Figs. 2h,i and 3b,c), whereas the AMOC slowing (Fig. 5g) does not differ much in the final years despite the smaller trend in LR at 26°N. Although, the AMOC weakening is larger in LR than in HR and ER between 30° and 60°N centered around 1500-m depth (Figs. 5a,d,f). This puts a question mark to studies linking the strength of the warming hole directly to a slowing down of the AMOC (Caesar et al. 2018, using observations; Menary and Wood 2018; Rahmstorf et al. 2015). In this sense, Keil et al. (2020) have argued for multiple drives of the warming hole feature. During the historical period, the anthropogenically forced changes of both the gyre and overturning circulation induce heat transport increase out of the subpolar region to the Greenland–Iceland–Norwegian (GIN) Seas and then farther to the Arctic, contributing to the warming hole feature in the North Atlantic (Keil et al. 2020).

In the subpolar gyre, heat transport is driven by both gyre and overturning circulation. The strengthened barotropic circulation in high latitudes, where the northern part of the subpolar region and GIN Seas (Figs. 6a–c) can similarly contribute to the development of the warming hole and the associated sea level decline. Conversely, the AMOC effect is mitigated by a weaker strengthening of the circulation in vicinity of Greenland in ER (Figs. 6c,e) leading to a smaller DSL decrease and a smaller-scale warming hole in comparison to HR. The DSL decline and strengthening subpolar circulation are larger in LR than in HR and ER (Figs. 6d,f), despite the warming hole in LR being smaller (Fig. 2g and Fig. S1 in the online supplemental material). This could be because LR has a weaker GIN Seas circulation (Figs. 6a,d,f), which could indicate smaller heat transport out of the subpolar region. Future DSL change in the subpolar North Atlantic and the formation of the warming hole are hence resolution dependent.

Curry et al. (1998), Böning et al. (2006), and Häkkinen et al. (2011) show the impact of the surface wind stress on both subpolar gyre variability and the strength. The decline of the

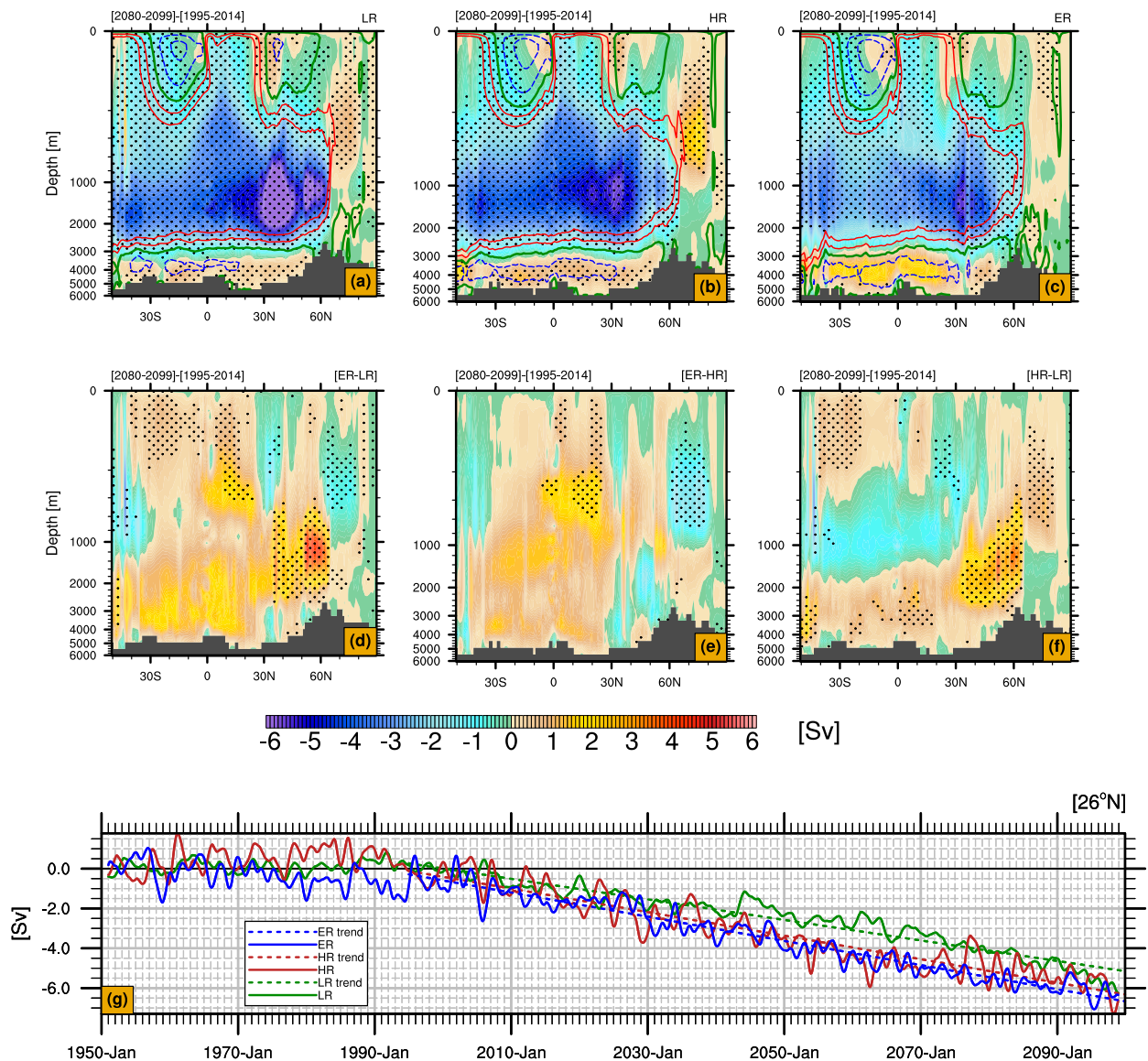


FIG. 5. Anomalies of the Atlantic meridional overturning circulation streamfunction (Sv) for (a) MPI-ESM-LR, (b) MPI-ESM-HR, and (c) MPI-ESM-ER, each for the time mean differences over historical simulation and SSP5-8.5. Differences of the anomalies between the models: (d) ER minus LR, (e) ER minus HR, and (f) HR minus LR. The contours represent the historical mean (1995–2014; contour interval is 3 Sv). The contour colors denote solid red for the positive values, green line for the zero contour, and dash blue for the negative values. In all panels stippling indicates statistically significant differences (95% confidence level). (g) Time series of 3-yr running mean AMOC streamfunction (Sv) relative to 1950s at 1000 m and 26°N. Dashed lines represent a linear trend over the period 2030–99 for LR, HR, and ER, plotted in green, red, and blue, respectively.

surface wind stress over the subpolar gyre region could result in the spindown of the subpolar gyre circulation, leading to sea level increase (Chafik et al. 2019; Putrasahan et al. 2019). A noticeable difference between eddy-rich and lower resolutions is that wind stress reduces in ER over the subpolar North Atlantic (50°–65°N) in contrast to LR and HR (Figs. 3j,k), for which wind stress intensify (Fig. 4c). These changes agree with the noted spindown of the subpolar gyre in ER and the strengthened gyre circulation in LR and HR (Figs. 6a–c). However, the extensive spread in zonal mean zonal wind stress

anomalies implies a minor resolution dependency in subpolar gyre region (Fig. 4c) at the 95% significant level.

Dynamically, the simplest concept for the barotropic circulation is the balance between wind stress curl and the advection of vorticity which is described by the Sverdrup streamfunction. For the time-mean circulation the validity of the concept has been approved for interior of the subtropical circulation (e.g., Sonnewald et al. 2019; Wunsch and Roemmich 1985; Wunsch 2011). The degree of the Sverdrup concept's validity to describe temporal changing circulation changes was previously

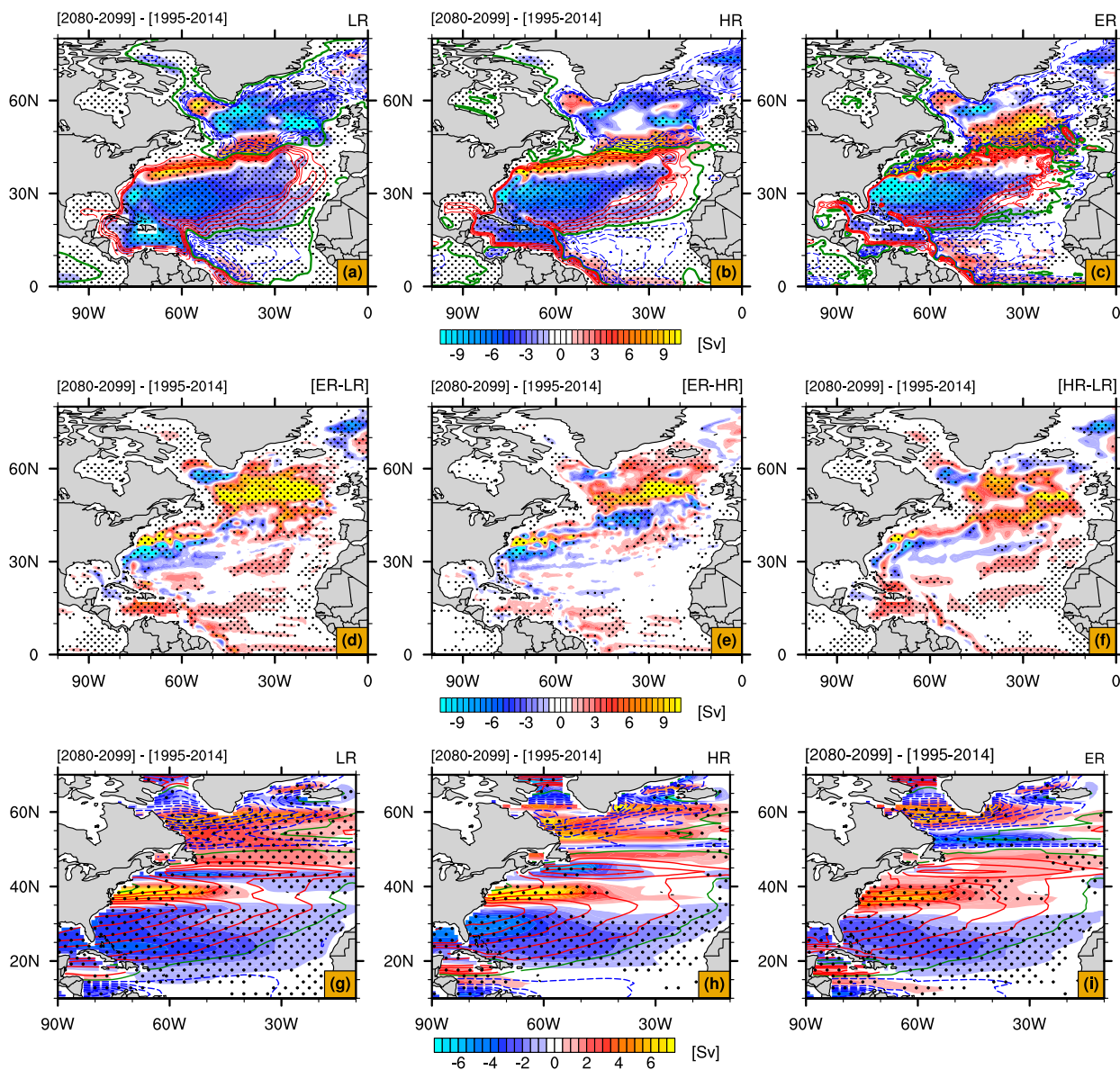


FIG. 6. Anomalies of (a)–(c) barotropic streamfunction and (g)–(h) Sverdrup streamfunctions for the SSP5-8.5 (2080–99) average relative to the historical simulation, averaged over 1995–2014 in North Atlantic for MPI-ESM-LR in (a) and (g), MPI-ESM-HR in (b) and (h), and MPI-ESM-ER in (c) and (i); the differences of the anomalies between the models: (d) ER minus LR, (e) ER minus HR, and (f) HR minus LR. The contours represent the historical mean [1995–2014; contour intervals are 2 Sv in (a)–(c) and 5 Sv in (g)–(h)]. The contour colors denote solid red for the positive values, green line for the zero contour, and blue dashed for the negative values. The stippling indicates the statistically significant regions at the 95% confidence level.

demonstrated (e.g., Willebrand et al. 1980; Hautala et al. 1994; Stammer 1997; Morris et al. 1996, Thomas et al. 2014) and an agreement was found even outside of the subtropics. The Sverdrup streamfunction was calculated in the North Atlantic and North Pacific (Figs. 6, 9) to quantify the impact of the wind stress curl. The weakening of the North Atlantic Subpolar Gyre between 50° and 60°N can be explained by the weakening of surface wind stress curl in ER (Fig. 6i). Despite the strengthened circulation (Figs. 6a,b, 4b) and slightly intensified surface wind stress (Fig. 4c) in LR and HR, their curl weakens in both

models (Figs. 6g,h). The changes in subpolar gyre circulation do not entirely concur with the Sverdrup dynamics in HR, although HR and ER have the same T127/L95 atmospheric component.

All three resolutions show a weakening subtropical gyre (Figs. 6a–c), associated with a negative DSL, and just north of the Gulf Stream a band of positive DSL (Figs. 3a–c) that signifies the reduction of Gulf Stream transport associated with the weakening subtropical gyre and the declining AMOC (Fig. 5g). The weakening of the Gulf Stream under warming

conditions during the twenty-first century (Yang et al. 2016) could be related to the sea level changes in the North Atlantic associated with higher sea level rise north of the Gulf Stream (Bouttes et al. 2014; Chen et al. 2019; Levermann et al. 2005; Yin et al. 2009). The argument requires that the DSL is lower than the global mean such that a relaxation locally leads to a DSL rise; the same applies to the barotropic streamfunction.

ER shows the largest DSL reduction in the subtropical gyre (Figs. 3d,e), although a weakening of wind stress is smaller south of 40°N (Figs. 3j,k, 4c). However, the spindown of the subtropical gyre is larger in the ER compared to HR and LR (Figs. 6d,e, 4b). There is no considerable difference in the AMOC slowdown (Figs. 5e,g) between HR and ER. The AMOC deceleration is larger by 0.25 Sv in ER than in HR and 1.25 Sv than in LR (Fig. 5g) by 2100 at 26°N. The AMOC linear trend, calculated over 1995–2099, amounts to -0.061 Sv yr⁻¹ for ER, -0.059 Sv yr⁻¹ for HR, and -0.052 Sv yr⁻¹ for LR. Despite the similar magnitude of AMOC decline at 26°N in HR and ER, spindown of the subtropical gyre and the DSL reduction is larger in ER than in HR.

In addition to the effect of AMOC slowdown, changes in wind stress could also be responsible for the sea level reduction in the subtropical gyre south of the Gulf Stream (40°N), as suggested by Bouttes et al. (2012). The Sverdrup circulation of the North Atlantic Subtropical Gyre weakens dramatically in all three models. Moreover, the wind stress weakens south of 40°N in the zonal mean, with a stronger decline in HR and LR relative to the ER (Fig. 4c). The associated Sverdrup circulation is illustrated in Figs. 6g–i for comparison with the gyre changes as illustrated by the barotropic streamfunction (Figs. 6a–c, 4b). Additionally, the contours representing the present-day state are superimposed over the streamfunction anomalies to better visualize the shifting and changing of gyres. The wind stress curl changes tend to weaken the gyre circulation in the southern part of the North Atlantic Subtropical Gyre, whereas the northern part experiences a strengthening in all model versions (Figs. 6g–i). This suggests a poleward shift of the weakening subtropical gyre and Gulf Stream (Figs. 6a–c).

b. North Pacific

In contrast to the North Atlantic, in ER the DSL increases south of the Kuroshio Extension (over the subtropical gyre) and decreases farther to the north (in the subpolar gyre, Fig. 7a). This characteristic North Pacific dipole pattern is opposite to that in the North Atlantic and its axis is located along the steep DSL gradient associated with the Kuroshio causing further steepening of the frontal zone. In the southern part of the subpolar gyre, the DSL reduction is much greater in ER and HR than in LR (Figs. 7d,f), though there is no substantial difference between HR and ER (Fig. 7e). The DSL decreases in the lower resolutions along the eastern boundary of the North Pacific (Figs. 7a,b), while ER shows an increase in the Gulf of Alaska (Figs. 7c). The discrepancies between the models are negligible in the northern part of the subpolar gyre (Figs. 7d–f). In the subtropical gyre, the DSL increase is larger in ER compared to the LR and HR (Figs. 7d,e), and in HR than in LR (Fig. 7f), along

with a significant increase east of Japan in the eddy-rich model (Fig. 8a).

In HR and ER, the subpolar gyre strengthens (Figs. 9a,b), but in LR, the barotropic streamfunction field exhibits only minor change (Fig. 9c). Although the subpolar gyre is stronger in ER than in LR, the differences in subpolar gyre circulation between the models are relatively insignificant (Figs. 9d–f). The changes in the subtropical gyre indicate a pattern with a positive north and negative south parts of the gyre (Figs. 9a–c). The northern part of subtropical gyre (the Kuroshio region) strengthens; here ER displays a considerable amplification (30°–35°N; Fig. 8b). In the same region, we also noticed the high rate of DSL changes (Fig. 8a). Although the streamfunction differences are significant between the eddy-rich and eddy parameterized models in the northern part of the subtropical gyre (Figs. 9d,e), weakening southern part shows minor changes (Figs. 9d,e). The differences between LR and HR are significant (insignificant) in the southern (northern) part of the subtropical gyre circulation (Fig. 9f).

In comparison to the DSL change, changes of the barotropic circulation (Figs. 9a–c) show some distinctively different patterns in the tropical regions. Although, the DSL changes across the Kuroshio Extension front are still reflected by similar albeit much weaker streamfunction changes, the strengthening of the subtropical gyre encompasses only the region 30°–40°N, while for DSL it reaches down to 20°N. The negative DSL change south of 20°N covers the entire tropical region, while for the streamfunction it reaches down to only 15°N, where the pattern continues southward by a positive signal. Streamfunction and DSL are therefore inconsistent in the region north of the equator until 30°N, a region where the Pacific and the Indian Ocean are connected by the Indonesian Throughflow passages (Zhang et al. 2014).

Because of the absence of deep-water formation and deep convection in the North Pacific, similar changes seen in CMIP5 models were mainly attributed to changes in the wind field (Sakamoto et al. 2005; Yin et al. 2010). Merrifield (2011) has shown the relevance of off-equatorial wind changes for explaining the features of the large observed sea level trend in the western tropical Pacific during the 1990s and early 2000s. Figure 8c depicts the zonally averaged zonal wind stress changes for three models, showing an increase north of about 38°–45°N and a decrease to the south. Although differences in wind stress change between the models are not significant at the 95% confidence interval of the multimember mean, ER shows less weakening in the subtropical and more strengthening in the subpolar in comparison to HR and LR (Figs. 7j,k, 8c).

Changes in wind stress curl were found to explain the intensification of the subtropical gyre in the South Pacific since the early 1990s (Roemmich et al. 2007, 2016), which were also shown by Köhl and Stammer (2008) to explain the sea level trends during the longer time scale 1960–2001 over much of the Pacific Ocean. We will therefore again examine the wind-driven component of the circulation by the Sverdrup streamfunction (Figs. 9g–i).

Consistent with the barotropic streamfunction, the Sverdrup circulation changes show that the southern part of the North Pacific Subtropical Gyre weakens in all models, while

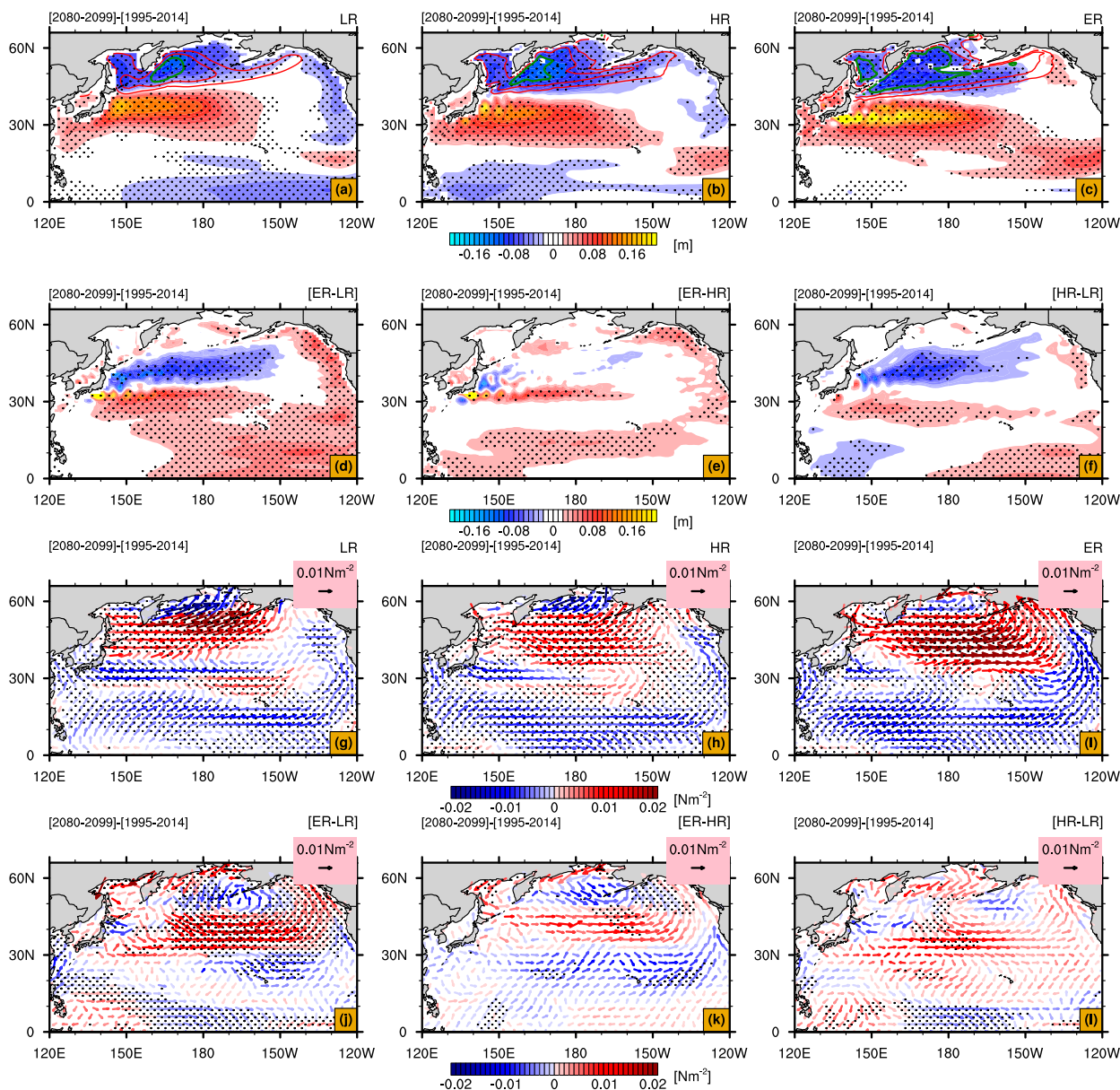


FIG. 7. As in Fig. 3, but for the North Pacific.

the northern part of the gyre (north of 30°N) indicates a strengthening (Figs. 9g–i). Cheon et al. (2012) argue that this pattern (positive north part and negative south part) observed in the subtropical gyre indicates a poleward shift rather than a strengthening of the gyre under a warming future. Yin et al. (2010) further corroborate this hypothesis of the subtropical gyre poleward shift, resulting from the poleward shift of subtropical high in the western Pacific and the associated wind system. These characteristic patterns of DSL change in the western North Pacific because of the poleward shift and intensification of the Kuroshio have also been studied earlier in earlier CMIP models (e.g., Church et al. 2013a,b; Fox-Kemper et al. 2021; Sueyoshi and Yasuda 2012; Suzuki and Tatebe 2020; Terada and Minobe 2018; Yin 2012; Zhang et al. 2014).

However, whether this pattern in the Sverdrup and barotropic streamfunction indicates a poleward shift of the subtropical gyre or a strengthening of the Kuroshio is debatable (see section 4d). Different from the other resolutions, in LR, Sverdrup circulation weakens in the southern part of the North Pacific Subpolar Gyre, while the northern part shows a strengthening (Fig. 9g). It significantly strengthens in ER, and crosses the present-day zero contour (Fig. 9i), while HR shows no considerable change (Fig. 9h).

Previous studies have emphasized that increased model resolution is necessary for the representation of accurate western boundary currents such as Gulf Stream, Kuroshio, and East Australian Currents (e.g., Chassignet and Xu 2017; Chassignet et al. 2020; Griffies et al. 2015; Hewitt et al. 2017, 2020; Roberts et al. 2018;

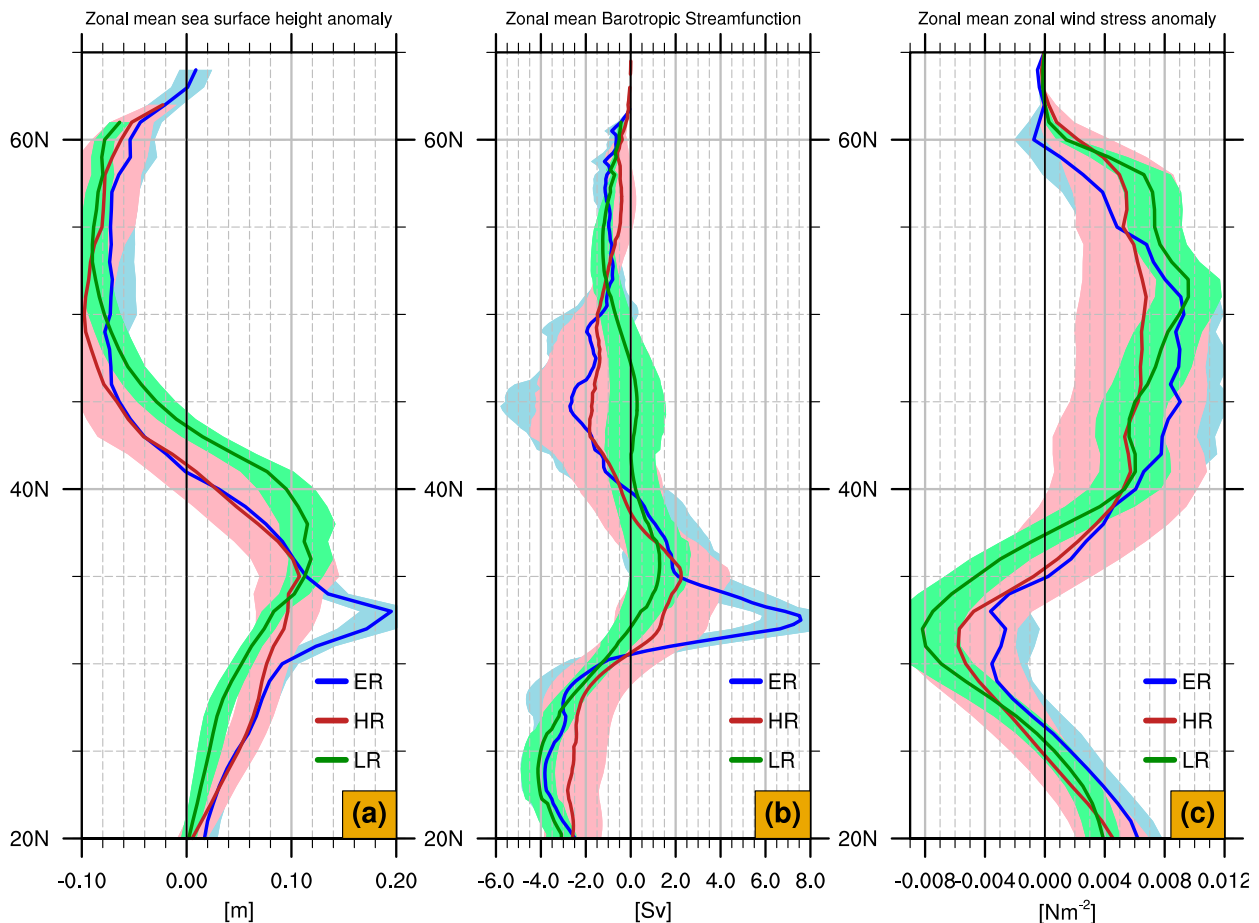


FIG. 8. As in Fig. 4, but for the North Pacific.

Small et al. 2014). Similarly, Hurlburt et al. (1996) and Nishikawa et al. (2020) demonstrate that eddy-rich horizontal resolution can realistically represent the Oyashio–Kuroshio fronts. Therefore, the strong, narrow current, noted in the DSL and barotropic streamfunction fields (Figs. 7, 9) east of Japan, denotes the more accurately represented Kuroshio in the eddy-rich model, which alters the characteristics of the Kuroshio–Oyashio front by representing a significant number of mesoscale activities in comparison to eddy parameterized models. The Kuroshio, between 30° and 35°N, is significantly intensified in the ER model but slightly strengthens in the high-resolution and the low-resolution climate models.

c. The Southern Ocean

Like in the North Atlantic and North Pacific, a north–south gradient of DSL change is found in the Southern Ocean for all resolutions (Figs. 10a–c), with increasing sea level north to ~50°S and decreasing south of ~50°S, which has been described as a belt-like pattern (Yin et al. 2010). The increase (decrease) of DSL north (south) of the ACC is smaller in ER than in HR and LR at the end of the twenty-first century (Figs. 11a,b, 12a). In earlier studies, the strengthening and poleward shift of Southern Hemisphere westerlies have been

shown to induce such a pattern of DSL changes, although it was also noted that it is not sufficient to explain all of the projected changes (Thompson and Solomon 2002; Bouttes et al. 2012; Frankcombe et al. 2013).

The projected wind stress change shows a decrease north of the ACC, with a peak around 38°S, and an increase to the south centered around 58°S (Figs. 10g–i, 12c). This dipole-type pattern in the zonal component of the wind stress is interpreted by Fyfe and Saenko (2006) as the strengthening and poleward shift. The differences in wind stress between ER and HR are minor (Figs. 11h, 12c). The changes in LR are considerably larger than both ER and HR (Figs. 11g,i, 12c).

The pattern of DSL reflects circulation changes characterized by similar patterns of barotropic streamfunction change (Figs. 10d–f). The intriguing feature of the projected circulation change is an intensifying region centered around 45°S (Fig. 12b). This strengthening could be caused by a potential southerly shift of subtropical gyres, and as horizontal resolution improves, the magnitude of the strengthening decreases. The poleward shift in sea surface height contours is consistent with regional sea level rise patterns (Gille 2014). Therefore, understanding gyre shift is crucial for sea level change studies. The historical mean contours overlaid over the anomalies can

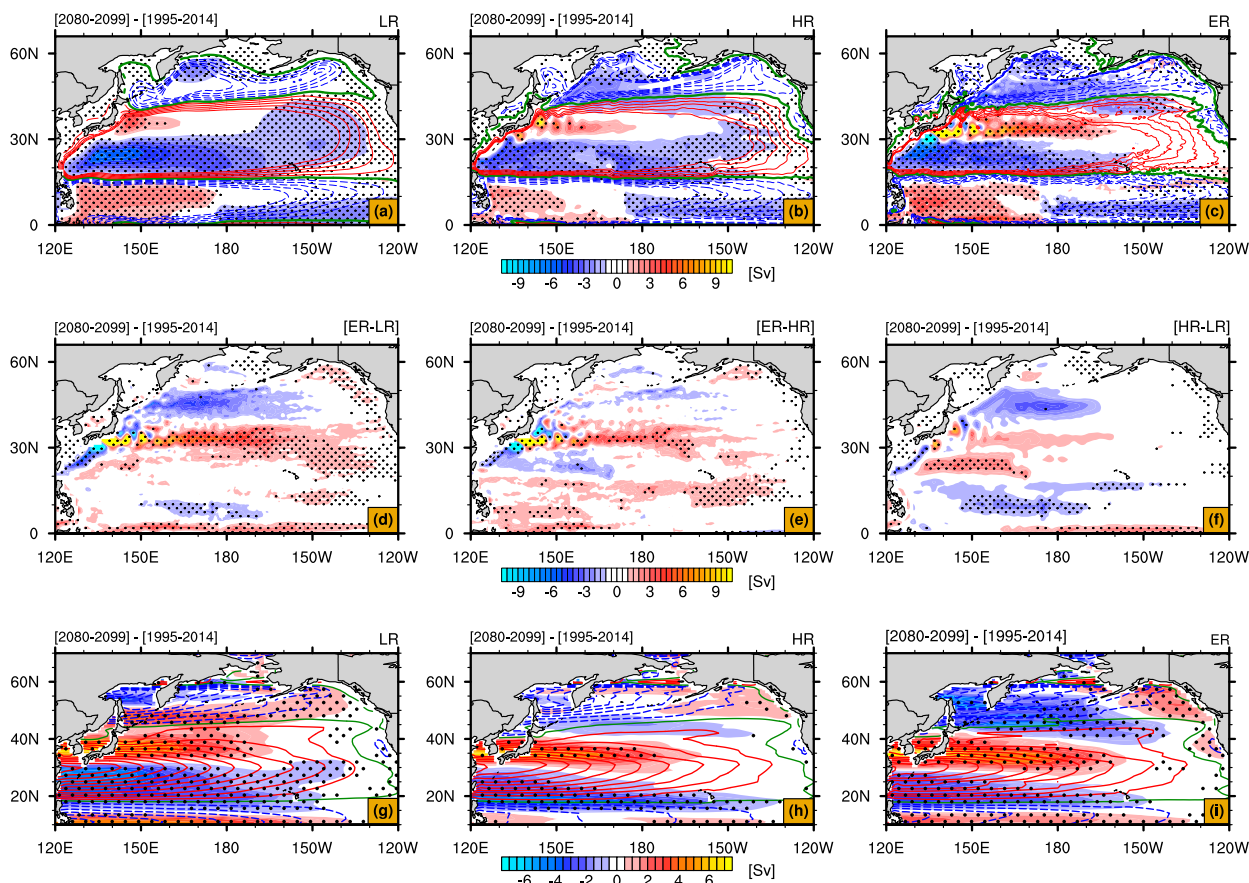


FIG. 9. As in Fig. 6, but for the North Pacific.

further explain this poleward movement (Figs. 10a–e). Positive dynamic sea level anomalies and negative anomalies in the barotropic streamfunction field both cross the present-day zero contour, which indicates a poleward shift. This poleward shift of subtropical gyres, interpreted as the belt-like pattern, is less pronounced in ER than in HR and LR (Figs. 10d,e). Similarly, ER reflects a thinner belt of DSL increase compared to HR and LR (Figs. 10a,b).

A dipole-like pattern of changes in the southern Indian Ocean and South Atlantic Ocean is revealed by changes in streamfunction for the Southern Ocean (Figs. 10d–f). The southern (northern) part of the Indian Ocean Gyre is shown to be strengthening (weakening) by around 18 Sv (10 Sv) in the ER. The southern part of the South Atlantic Gyre is also strengthening by about 13 Sv (Fig. 10f). However, the South Pacific Gyre weakens in all the projections by about 6 Sv. When the changes in subpolar gyres are taken into account, we found that all projections show a weakening Weddell Gyre (Fig. 10d–f), which is more pronounced in HR than in LR and ER (Figs. 11e,f). With a larger acceleration in ER (Fig. 11d), the Ross Gyre strengthens in LR and ER (Figs. 10d,f), whereas it weakens in HR (Fig. 10e).

Eddies are omnipresent in the Southern Ocean, especially along the ACC (e.g., Constantinou and Hogg 2019; Frenger et al. 2015). These eddies are crucial for establishing the

stratification in the presence of wind and buoyancy forcing (Karsten et al. 2002). The intensified Southern Hemisphere westerlies enhance the Southern Ocean eddy activity, leading to the phenomenon known as eddy saturation (Straub 1993) and eddy compensation. As a result, the strength of the ACC, the isopycnal slope, and the meridional circulation of the Southern Ocean become less sensitive to the enhanced forcing. Studies using higher-resolution ocean models (e.g., Farneti et al. 2010; Hallberg and Gnanadesikan 2006; Meredith and Hogg 2006) or observations (Böning et al. 2008; Chidichimo et al. 2014; Firing et al. 2011) have shown the insensitivity of ACC or the Southern Ocean meridional overturning circulation to the enhanced westerlies. They stated that the non-eddy-resolving models respond with an accelerated ACC, steeper isopycnals, and robust meridional overturning circulation to wind intensification forcing changes.

To evaluate the response of ACC to the intensified westerly wind stress, we investigated the Drake Passage transport independently for the two time periods (Fig. 13a). Even though the studies cited above oppose the ACC's sensitivity to changing westerly winds, we discovered an accelerating ACC particularly in our eddy-rich model (Fig. 13b). With a substantial increase in ER, the strength of the ACC increases in ER and LR (Fig. 13a). The LR reveals increased transport between 60° and 68°S, with no changes north of 60°S. The transport in

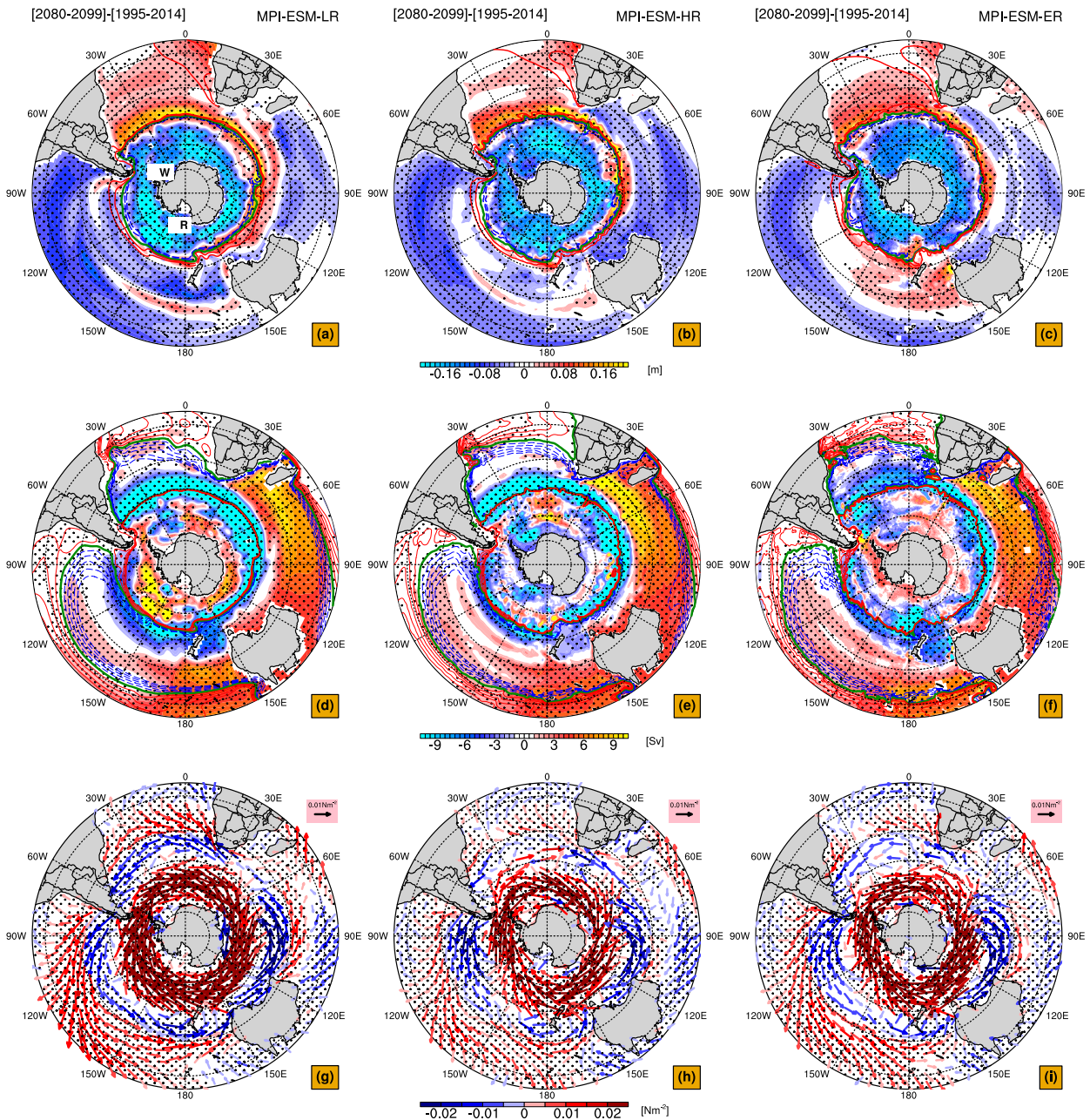


FIG. 10. Anomalies of (a)–(c) dynamic sea level, (d)–(f) barotropic streamfunction, and (g)–(i) wind stress for the SSP5-8.5 (2080–99) average relative to the historical simulation, averaged over 1995–2014 in Southern Ocean for (left) MPI-ESM-LR, (center) MPI-ESM-HR, and (right) MPI-ESM-ER. The contours represent the historical mean [1995–2014; contour intervals are 0.1 m in (a)–(c) and 2 Sv in (d)–(f)]. The contour colors denote solid red for the positive values, green line for the zero contour, and blue dashed for the negative values. The stippling indicates the statistically significant regions at the 95% confidence level. In (a), W stands for Weddell Sea and R stands for Ross Sea.

HR remains unchanged until 64°S, south of which it begins to weaken (Fig. 13a), reflecting its insensitivities to accelerated southern westerlies. Furthermore, Shi et al. (2021) and Swart et al. (2018) show that factors other than wind influence the Southern Ocean circulation. Warming in the upper ocean generates a density change, accelerating the ACC. Heat and

freshwater fluxes at the surface could also cause changes observed in ER.

The stronger DSL increase relative to HR and LR is significant in ER in the South Pacific (25°–60°S), especially east of Australia (Figs. 11a,b). The East Australian Current system strengthens as DSL rises in the ER model (Figs. 11d,e).

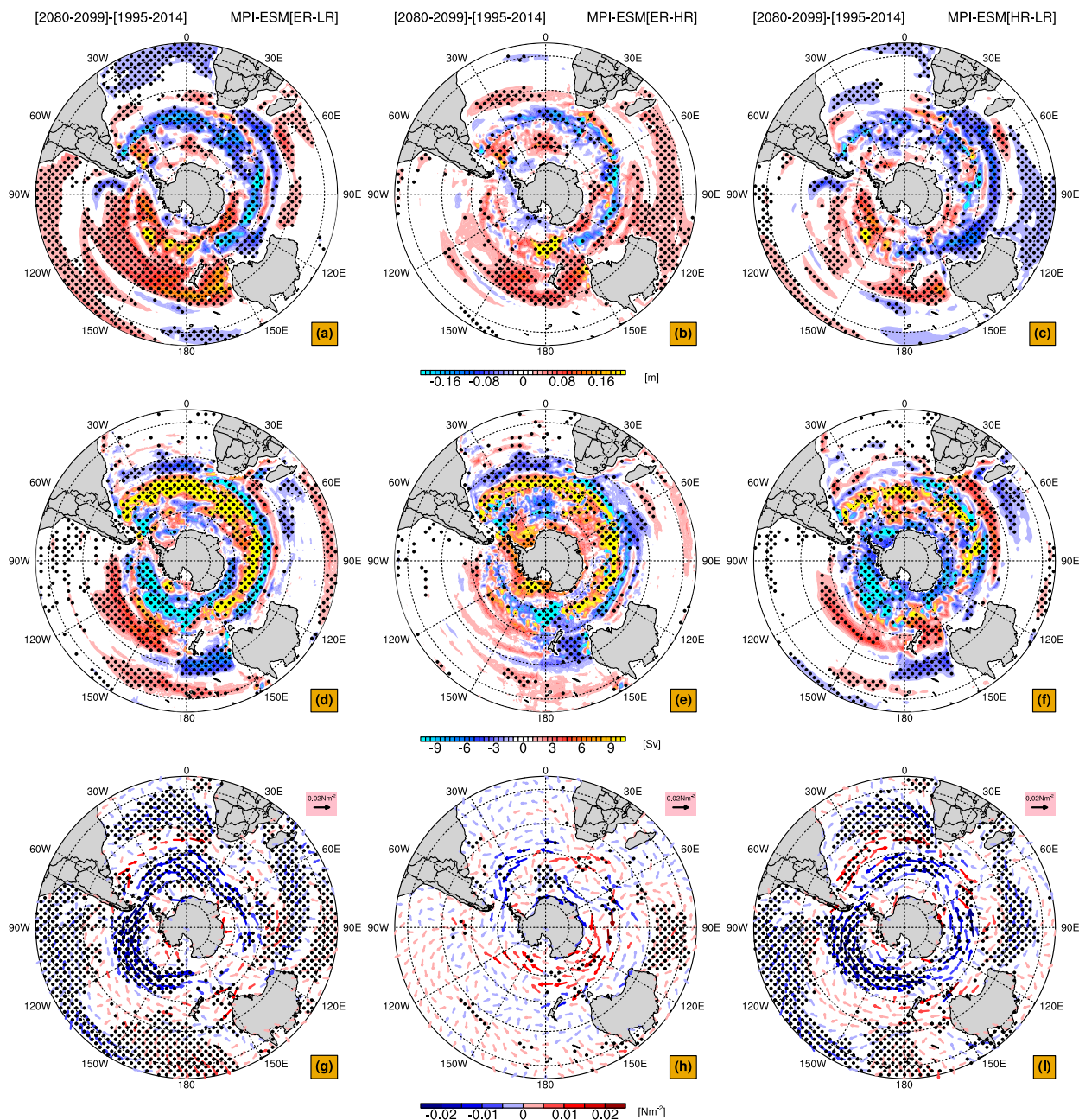


FIG. 11. Differences of the anomalies between the models [(left) ER minus LR, (center) ER minus HR, and (right) HR minus LR] for (a)–(c) dynamic sea level, (d)–(f) barotropic streamfunction, and (g)–(i) wind stress in Southern Ocean. The stippling indicates the statistically significant regions at the 95% confidence level.

This intensified circulation represented by the barotropic streamfunction field is more significant in ER than in HR and LR. Lower-resolution models poorly simulate the western boundary current system due to unresolved mesoscale processes, whereas the East Australian Current is adequately simulated in ER. Increasing southward transport of the East Australia Current in a warming climate was shown to be a response to the intensified South Pacific wind stress curl (Goyal et al. 2021; Roemmich et al. 2007), which can be

seen in ER. We also found the enormously increased sea surface temperature in southeastern Australia in ER as indicated in previous studies (Wu et al. 2012; Hobday and Pecl 2014), which causes this region to be a global warming hotspot.

The DSL decreases in southern Indian Ocean and the Pacific (north of 30°S), though it increases in the Atlantic (Figs. 10a–c). The increase in the South Atlantic is larger in LR than in HR as well as ER (Figs. 11a,c). In the south Indian Ocean, the DSL

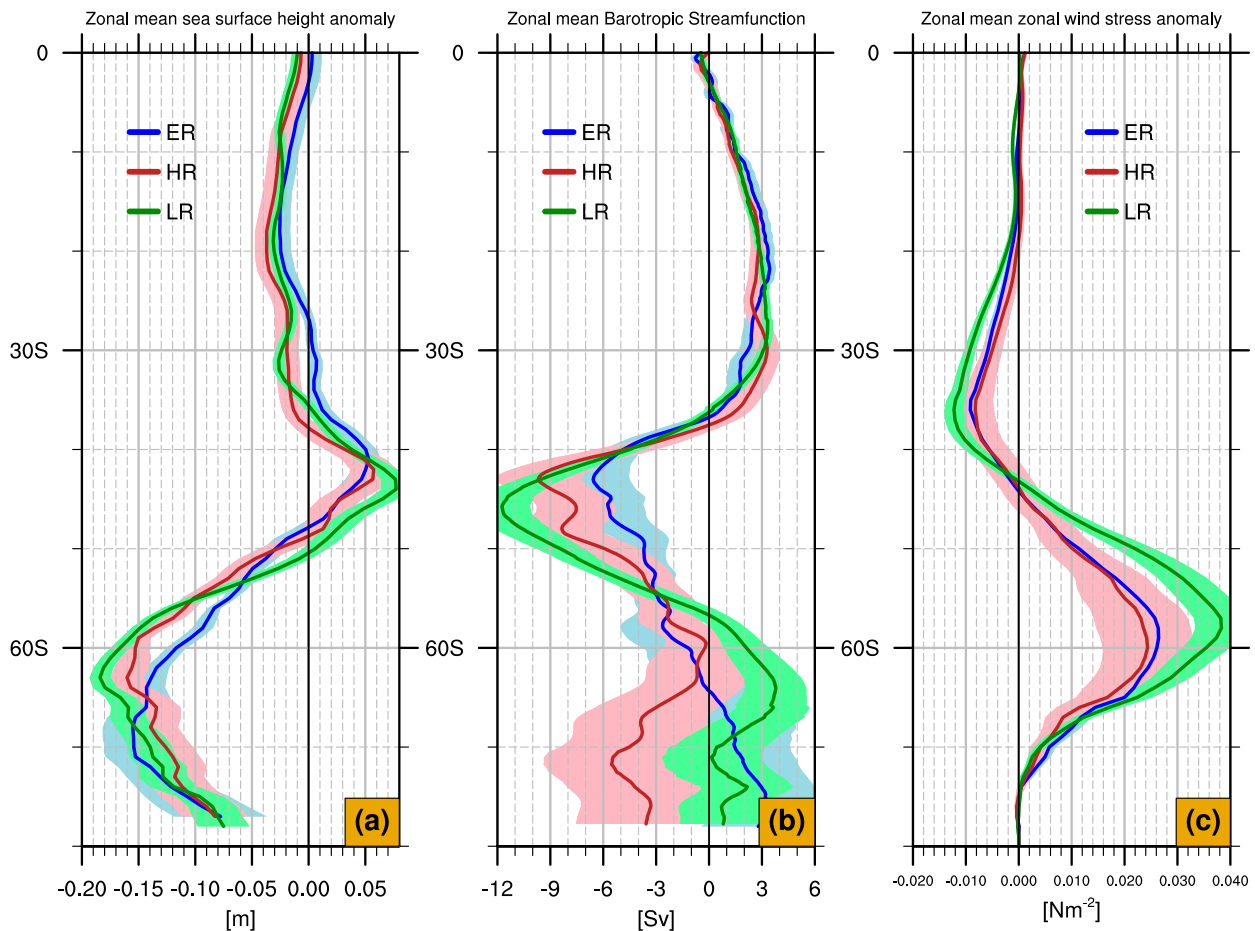


FIG. 12. As in Fig. 4, but for the Southern Ocean.

decreases, in order of decreasing the reduction, in HR, LR, and ER (Figs. 11a–c), similarly in the South Pacific.

d. Displacement of major ocean gyres

The poleward shift of major ocean gyres, which secondarily drives sea level change, was previously discussed by Yang et al. (2020). To comprehend how differences in poleward shift affect different DSL responses, we have calculated the change in position of major ocean gyres in the three versions of MPI-ESM and quantified the linear trend from 2030 to 2100 in Fig. 14. Most gyres shift toward the poles (except for the North Pacific), indicating a statistically significant poleward gyre displacement as a response to a warmer climate.

The poleward shift of the North Atlantic Subtropical Gyre is almost identical in all projections, showing a magnitude of 0.0138° , 0.0112° , and 0.0161° per year in ER, HR, and LR, respectively (Fig. 14b). The North Atlantic Subpolar Gyre, on the other hand, responds differently in each projection, with the highest displacement in ER and trends of 0.0129° , 0.0125° , and 0.0085° per year in ER, HR, and LR, respectively (Fig. 14a), from 2030 to 2099.

Periods over which trends occur are also not very consistent. While HR shows no trend until the last few decades,

poleward trends start in the early to mid-twenty-first century for LR and ER, respectively, but it seems to cease after 2070 for ER pointing to considerable influence of climate variability. The North Pacific Subpolar Gyre behaves contrarily to the North Atlantic in ER, which shows a southward shift, indicated by a negative trend of 0.0088° per year, while northward shifts are small with 0.0067° per year in HR and 0.0011° per year in LR (Fig. 14c). Similarly, North Pacific Subtropical Gyre displacements are also relatively small in HR and LR, with linear trends of 0.0028° and $0.0010^\circ \text{ yr}^{-1}$, respectively (Fig. 14d). Both poleward shifts of the ocean gyres in the North Pacific are not statistically significant in LR, and in ER, the subtropical gyre is experiencing a statistically insignificant downward trend of $0.0026^\circ \text{ year}^{-1}$.

The displacements of the North Pacific Subpolar and Subtropical Gyres are negligible when compared to interannual variability in all configurations (Figs. 14c,d). Consistent with the changes of the barotropic streamfunction (Figs. 9c), the boundary of the negative circulation anomaly crossing the zero contour of present day (solid green line) in the Sverdrup circulation implies that the North Pacific Subpolar Gyre strengthens and moves southward in ER (Fig. 9i). Thus, ER

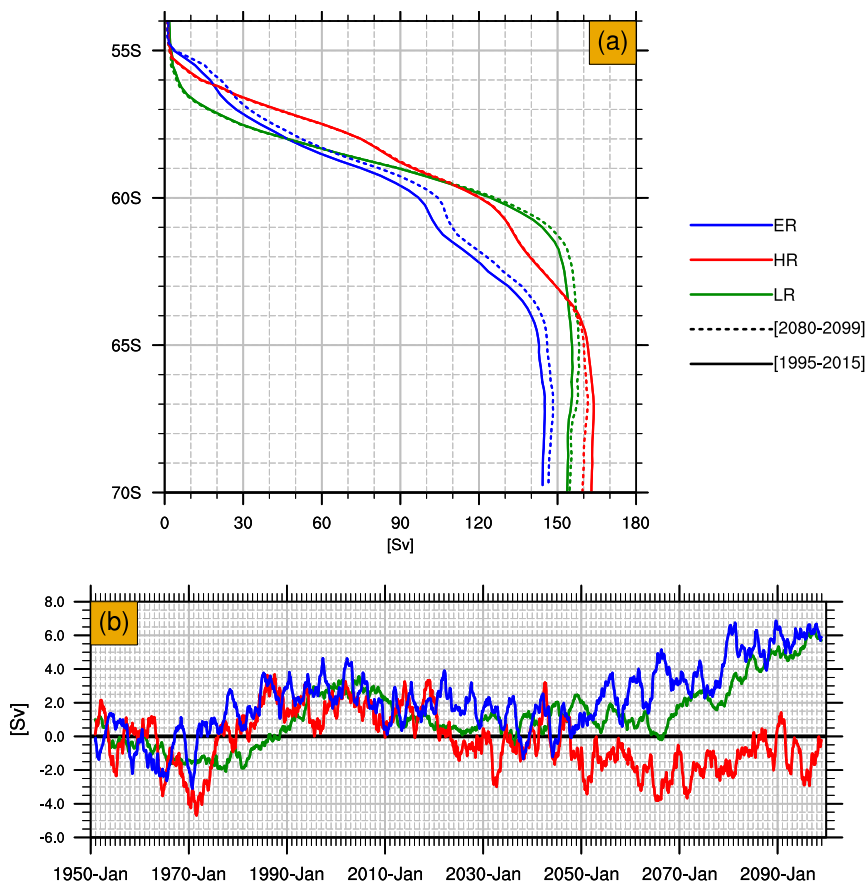


FIG. 13. (a) Time mean transport through Drake Passage; the dashed line for the time mean future (2080–99) transport and the solid line indicates the historical (1995–2014) transport (Sv). (b) Time series of ACC transport through Drake Passage relative to 1950s mean at 65°W. The green, red, and blue lines represent MPI-ESM-LR, MPI-ESM-HR, and MPI-ESM-ER, respectively. The positive barotropic streamfunction values were considered for the calculation.

shows a strengthening Kuroshio due to the stronger wind rather than a poleward displacement (Fig. 14d), despite the interpretation of earlier CMIP5 model investigations that the changes in the Sverdrup streamfunction indicates a northward movement of the subtropical gyre (Cheon et al. 2012). It is worth mentioning that the latitudinal variations observed in the North Atlantic Subtropical Gyre are consistent with a pattern of positive north and negative south parts of the gyre in the Sverdrup streamfunction field (Figs. 6g–i) and barotropic circulation (Figs. 6a–c).

Our results indicate a distinct poleward shift of the ACC (Fig. 14e), which has been linked to climate change in many earlier studies (e.g., Morrow et al. 2008; Yang et al. 2020). Interestingly, the eddy-rich model shows less poleward migration of the ACC with induced transport increase in comparison to the high- and low-resolution models. Between 2030 and 2100, the HR has the highest trend of $0.0044^{\circ} \text{ yr}^{-1}$, whereas the LR has the lowest trend of $0.0024^{\circ} \text{ yr}^{-1}$, while ER's linear trend lies with $0.0028^{\circ} \text{ yr}^{-1}$ in between. In ER, the latitudinal displacement of the ACC is less than in HR and LR (Fig. 14e), and we also observed the smallest poleward shift of

the ACC in the barotropic streamfunction (Figs. 11c,d) and sea surface height field (Figs. 11a,b).

The differences between the anomalies seen in the Arctic Ocean are not thoroughly covered in a separate section. Thus, the discrepancies found are outlined here at the end of the section 4. We noted a dipole pattern of the difference in the DSL changes between ER and the lower-resolution models in the Arctic Ocean (Fig. S5). The ER reveals no changes to the north of Greenland, where we diagnose strong sea level increase in HR and LR (Fig. 2c and Fig. S2i). As expected, the model differences of the freshwater content change show a similar behavior to the differences of sea level change (Fig. S6). Although the Beaufort Gyre weakens (Figs. 2d,e and Figs. S3d,e) at the end of the twenty-first century, our models, HR and LR, show a DSL increase in the Canada Basin (Figs. 2a,b) associated with freshwater accumulation (Fig. S7). Furthermore, we do not find any considerable changes in the wind stress field, except for its increase in the Chukchi Sea in ER (Fig. 2j and Fig. S4). The induced anticyclonic circulation in ER (Fig. 2f) causes the increase in DSL (Fig. 2c) and freshwater content (Fig. S7i) in the Canada Basin.

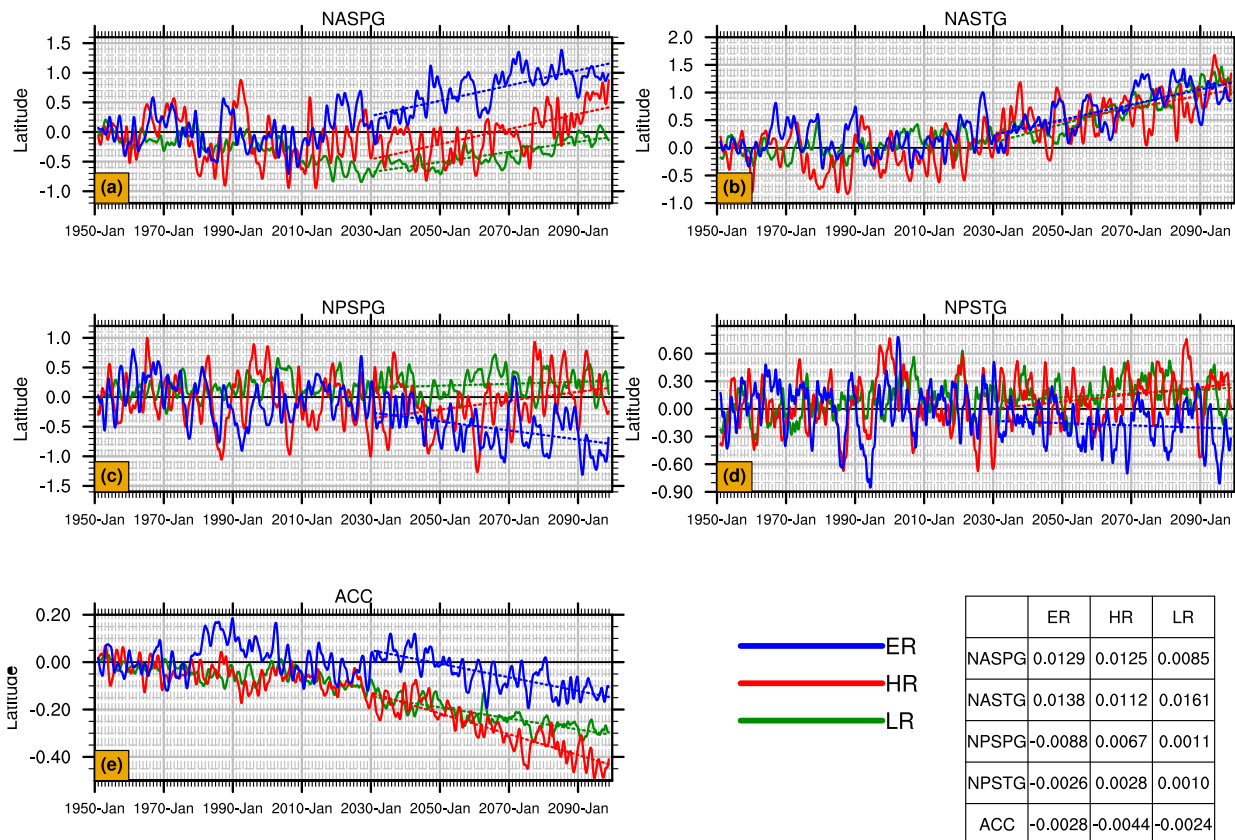


FIG. 14. Time series of 3 yr running mean latitudinal variations of the ocean gyres relative to the 1950s mean ($^{\circ}$). The position is calculated based on the barotropic streamfunction weighted center of each gyre, and the contours between the minimum and maximum eastward transport in the Drake passage were considered to calculate the mean central latitude of ACC transport. Abbreviations in each panel are North Atlantic Subpolar Gyre (NASPG), North Atlantic Subtropical Gyre (NASTG), North Pacific Subpolar Gyre (NPSPG), North Pacific Subtropical Gyre (NPSTG), and Antarctic Circumpolar Current (ACC). The linear trend is indicated by the dashed lines between 2030 and 2099 for LR, HR, and ER in green, red, and blue, respectively. The related linear trends are presented in the box ($^{\circ} \text{yr}^{-1}$).

5. Summary and concluding remarks

By analyzing model simulations from eddy-rich (ER), high-resolution (HR), and low-resolution (LR) versions of MPI-ESM run under the SSP5-8.5 scenario forcing, we found substantial DSL change differences in the global ocean among the different resolutions. We note that HR and ER have the same atmospheric component, whereas LR also has a lower-resolution atmosphere. However, when comparing LR and HR, we cannot fully discriminate between the effects of resolution changes versus intrinsic changes of surface forcing in either simulation. This is because the response to changes in external forcing is a complex coupled phenomenon that depends on details of the surface boundary condition formulation. Because of this, even ocean models coupled to the same atmosphere (Semmler et al. 2021) show different regional or global expressions of such change as soon as ocean surface fields are different. Nevertheless, in many cases we can link the responses in sea level change to the different ocean resolution, in particular comparing the HR and ER versions of the model.

All models simulate a meridional dipole pattern of sea level change in the North Atlantic. This dipole pattern is identified by a larger sea level rise relative to the global mean in the subpolar region and sea level decrease in the subtropical region. However, southeast of Greenland, we identify a patch of sea level decline, which shrinks with the enhanced horizontal resolution. The warming hole feature is also located in the same area as the sea level decline, indicating a similar pattern of behavior, particularly in HR and ER. We have mainly focused on the changes in the circulation to examine the causes of these differences, since the long-term changes in sea level are linked to the changes in the circulation.

In HR and LR, the subpolar gyre strengthens in the barotropic streamfunction field, although its component driven by the wind stress curl weakens. The strengthening circulation in the subpolar region, on the one hand, can induce the heat transport out of the region into the GIN Seas and then farther north to the Arctic, forming NA warming hole. However, in this region the changes in wind stress curl in the subpolar region do not agree with the change in circulation in the eddy permitting models.

In the ER model, the subpolar gyre weakens in both barotropic and Sverdrup fields, as well as the region of the sea level decline becomes small. Furthermore, the magnitude of the sea level decline is also smaller in ER compared to HR and LR. The sea level increase over the rest of the subpolar gyre has been simulated by all the models. This increase becomes smaller in the eddy-rich model, indicating lower sea level in the Labrador Sea and north of Gulf Stream. This lower increase is caused by lower freshwater content in ER than in HR and LR. Previous studies have widely reported the relation between the uncertainty in twenty-first century sea level change in the North Atlantic and the variability in projected weakening of AMOC (Yin et al. 2009; Bouttes et al. 2014). We observed a significant AMOC decline in all the versions. This decrease is very similar in HR and ER at 26°N. However, the DSL changes in the North Atlantic are considerably different between these models. These results indicate that the North Atlantic DSL change is not responding as we anticipated to the weakening AMOC. The sea level decline in the subtropical region is larger in ER compared to HR and LR, caused by the larger weakening of the circulation in ER.

The poleward shift of North Atlantic Subtropical Gyre, which is also observed in the Sverdrup field as a pattern of positive north and negative south parts of the gyre, is considerable in all the models. However, the differences between models are not significant.

Interestingly, a pattern of positive north and negative south parts of the gyre identified in the Sverdrup streamfunction most likely indicates the strengthening of Kuroshio rather than the poleward shift of the subtropical gyre in the ER simulation, because the gyres in the North Pacific show a negligible poleward displacement. It is further explained by identifying a significant DSL change, robust circulation, and less reduction of wind stress in the Kuroshio region (30°–35°N). These robust changes are identified only in the eddy-rich model, because of the realistically represented western boundary currents.

It is well known that in the Southern Ocean changes in sea level correspond to changes in ACC and barotropic circulation (e.g., van Westen and Dijkstra 2021). Southern Ocean sea level change is smaller in ER, indicating a minor poleward shift of the ACC in comparison to HR and LR. The ACC, as in earlier studies, is known to be insensitive to the strengthening westerlies in the higher-resolution models that explicitly resolve eddies. One interesting result is that ACC strengthens in ER, but remains unchanged or slightly weakened in HR. The findings indicate that ER, as opposed to HR, appears to be more sensitive to strong westerlies.

The general understanding is that many low-lying coastal areas experience substantial threats from sea level rise due to their relatively low elevation above sea level. Figure 1 by Magnan et al. (2022) provides a detailed overview of the low-lying islands and coasts of the world. However, we have not included in-depth discussion about low lying coastal areas that are located in the Indian Ocean and southwest Pacific due to small model differences of DSL anomalies (maximum around ± 40 mm; see supplemental Figs. S8–S13). Interesting to note is that the differences of DSL change between HR and ER is

significant in these regions and larger than the difference between LR and ER.

It is expected that the eddy-rich models improve the representation of the eddy activities, providing more accurate and informative sea level change patterns over the following decades. In general, the DSL change pattern and dynamics are similar in eddy-rich compared to the coarser-resolution climate models in each ocean basin, suggesting that the coarser-resolution models will remain valid in understanding the sea level change patterns. On the other hand, the detailed, quantitative responses depend on the resolution. The robust changes found in MPI-ESM-ER suggest that improved resolution will have an impact on the interpretation of regional sea level change in the following decades. Therefore, the sea level projections of coarse-resolution models should be interpreted with caution, predominantly in the eddy active regions such as Kuroshio, ACC, Gulf Stream, and East Australian Current, and one should consider restrictions associated with limited climate model horizontal resolutions, when planning future adaptation and mitigation investments.

Acknowledgments. Funded in part by the German Research Foundation (DFG) as part of the Priority Programme SPP 1889 “Sealevel.” Dian Putrasahan provided the data from the ER model simulation with support of the DFG funded Excellence Cluster “CLICCS” of Universität Hamburg. Contribution to the Centrum für Erdsystemforschung und Nachhaltigkeit (CEN) of Universität Hamburg.

Data availability statement. The MPI-ESM ScenarioMIP data are available at <https://esgf-data.dkrz.de/projects/esgf-dkrz/>.

REFERENCES

- Böning, C. W., M. Scheinert, J. Dengg, A. Biastoch, and A. Funk, 2006: Decadal variability of subpolar gyre transport and its reverberation in the North Atlantic overturning. *Geophys. Res. Lett.*, **33**, L21S01, <https://doi.org/10.1029/2006GL026906>.
- , A. Dispert, M. Visbeck, S. R. Rintoul, and F. U. Schwarzkopf, 2008: The response of the Antarctic Circumpolar Current to recent climate change. *Nat. Geosci.*, **1**, 864–869, <https://doi.org/10.1038/ngeo362>.
- Bouttes, N., J. M. Gregory, T. Kuhlbrodt, and T. Suzuki, 2012: The effect of windstress change on future sea level change in the Southern Ocean. *Geophys. Res. Lett.*, **39**, L23602, <https://doi.org/10.1029/2012GL054207>.
- , —, —, and R. S. Smith, 2014: The drivers of projected North Atlantic sea level change. *Climate Dyn.*, **43**, 1531–1544, <https://doi.org/10.1007/s00382-013-1973-8>.
- Caesar, L., S. Rahmstorf, A. Robinson, G. Feulner, and V. Saba, 2018: Observed fingerprint of a weakening Atlantic Ocean overturning circulation. *Nature*, **556**, 191–196, <https://doi.org/10.1038/s41586-018-0006-5>.
- Chafik, L., J. E. Ø. Nilsen, S. Dangendorf, G. Reverdin, and T. Frederikse, 2019: North Atlantic Ocean circulation and decadal sea level change during the altimetry era. *Sci. Rep.*, **9**, 1041, <https://doi.org/10.1038/s41598-018-37603-6>.

- Chassignet, E. P., and X. Xu, 2017: Impact of horizontal resolution ($1/12^\circ$ to $1/50^\circ$) on Gulf Stream separation, penetration, and variability. *J. Phys. Oceanogr.*, **47**, 1999–2021, <https://doi.org/10.1175/JPO-D-17-0031.1>.
- , and Coauthors, 2020: Impact of horizontal resolution on global ocean–sea ice model simulations based on the experimental protocols of the Ocean Model Intercomparison Project phase 2 (OMIP-2). *Geosci. Model Dev.*, **13**, 4595–4637, <https://doi.org/10.5194/gmd-13-4595-2020>.
- Chemke, R., L. Zanna, and L. M. Polvani, 2020: Identifying a human signal in the North Atlantic warming hole. *Nat. Commun.*, **11**, 1540, <https://doi.org/10.1038/s41467-020-15285-x>.
- Chen, C., W. Liu, and G. Wang, 2019: Understanding the uncertainty in the 21st century dynamic sea level projections: The role of the AMOC. *Geophys. Res. Lett.*, **46**, 210–217, <https://doi.org/10.1029/2018GL080676>.
- Cheon, W. G., Y.-G. Park, S.-W. Yeh, and B.-M. Kim, 2012: Atmospheric impact on the northwestern Pacific under a global warming scenario. *Geophys. Res. Lett.*, **39**, L16709, <https://doi.org/10.1029/2012GL052364>.
- Chidichimo, M. P., K. A. Donohue, D. R. Watts, and K. L. Tracey, 2014: Baroclinic transport time series of the Antarctic Circumpolar Current measured in Drake Passage. *J. Phys. Oceanogr.*, **44**, 1829–1853, <https://doi.org/10.1175/JPO-D-13-071.1>.
- Church, J. A., and Coauthors, 2011: Revisiting the Earth’s sea-level and energy budgets from 1961 to 2008. *Geophys. Res. Lett.*, **38**, L18601, <https://doi.org/10.1029/2011GL048794>.
- , and Coauthors, 2013a: Correction to “Revisiting the Earth’s sea-level and energy budgets from 1961 to 2008.” *Geophys. Res. Lett.*, **40**, 4066–4066, <https://doi.org/10.1002/grl.50752>.
- , and Coauthors, 2013b: Sea level change. *Climate Change 2013: The Physical Science Basis*, T. F. Stocker et al., Eds., Cambridge University Press, 1137–1216, <https://doi.org/10.1017/CBO9781107415324.026>.
- Constantinou, N. C., and A. M. Hogg, 2019: Eddy saturation of the Southern Ocean: A baroclinic versus barotropic perspective. *Geophys. Res. Lett.*, **46**, 12 202–12 212, <https://doi.org/10.1029/2019GL084117>.
- Couldrey, M. P., and Coauthors, 2021: What causes the spread of model projections of ocean dynamic sea-level change in response to greenhouse gas forcing? *Climate Dyn.*, **56**, 155–187, <https://doi.org/10.1007/s00382-020-05471-4>.
- Curry, R. G., M. S. McCartney, and T. M. Joyce, 1998: Oceanic transport of subpolar climate signals to mid-depth subtropical waters. *Nature*, **391**, 575–577, <https://doi.org/10.1038/35356>.
- Drijfhout, S., G. J. Van Oldenborgh, and A. Cimadoribus, 2012: Is a decline of AMOC causing the warming hole above the North Atlantic in observed and modeled warming patterns? *J. Climate*, **25**, 8373–8379, <https://doi.org/10.1175/JCLI-D-12-00490.1>.
- Eyring, V., S. Bony, G. A. Meehl, C. A. Senior, B. Stevens, R. J. Stouffer, and K. E. Taylor, 2016: Overview of the Coupled Model Intercomparison Project phase 6 (CMIP6) experimental design and organization. *Geosci. Model Dev.*, **9**, 1937–1958, <https://doi.org/10.5194/gmd-9-1937-2016>.
- Farneti, R., T. L. Delworth, A. J. Rosati, S. M. Griffies, and F. Zeng, 2010: The role of mesoscale eddies in the rectification of the Southern Ocean response to climate change. *J. Phys. Oceanogr.*, **40**, 1539–1557, <https://doi.org/10.1175/2010JPO4353.1>.
- Firing, Y. L., T. K. Chereskin, and M. R. Mazloff, 2011: Vertical structure and transport of the Antarctic Circumpolar Current in Drake Passage from direct velocity observations. *J. Geophys. Res.*, **116**, C08015, <https://doi.org/10.1029/2011JC006999>.
- Fox-Kemper, B., and Coauthors, 2021: Ocean, cryosphere and sea level change. *Climate Change 2021: The Physical Science Basis*, V. Masson-Delmotte et al., Eds., Cambridge University Press, 1211–1362, <https://doi.org/10.1017/9781009157896.011>.
- Frankcombe, L. M., P. Spence, A. M. Hogg, M. H. England, and S. M. Griffies, 2013: Sea level changes forced by Southern Ocean winds. *Geophys. Res. Lett.*, **40**, 5710–5715, <https://doi.org/10.1002/2013GL058104>.
- Frenger, I., M. Münnich, N. Gruber, and R. Knutti, 2015: Southern Ocean eddy phenomenology. *J. Geophys. Res. Oceans*, **120**, 7413–7449, <https://doi.org/10.1002/2015JC011047>.
- Fyfe, J. C., and O. A. Saenko, 2006: Simulated changes in the extratropical Southern Hemisphere winds and currents. *Geophys. Res. Lett.*, **33**, L06701, <https://doi.org/10.1029/2005GL025332>.
- Gent, P. R., and J. C. McWilliams, 1990: Isopycnal mixing in ocean circulation models. *J. Phys. Oceanogr.*, **20**, 150–155, [https://doi.org/10.1175/1520-0485\(1990\)020<0150:IMOCM>2.0.CO;2](https://doi.org/10.1175/1520-0485(1990)020<0150:IMOCM>2.0.CO;2).
- Gervais, M., J. Shaman, and Y. Kushnir, 2018: Mechanisms governing the development of the North Atlantic warming hole in the CESM-LE future climate simulations. *J. Climate*, **31**, 5927–5946, <https://doi.org/10.1175/JCLI-D-17-0635.1>.
- Gille, S. T., 2014: Meridional displacement of the Antarctic circumpolar current. *Philos. Trans. Roy. Soc.*, **A372**, 20130273, <https://doi.org/10.1098/rsta.2013.0273>.
- Good, S. A., M. J. Martin, and N. A. Rayner, 2013: EN4: Quality controlled ocean temperature and salinity profiles and monthly objective analyses with uncertainty estimates. *J. Geophys. Res. Oceans*, **118**, 6704–6716, <https://doi.org/10.1002/2013JC009067>.
- Goyal, R., M. H. England, M. Jucker, and A. Sen Gupta, 2021: Response of Southern Hemisphere western boundary current regions to future zonally symmetric and asymmetric atmospheric changes. *J. Geophys. Res. Oceans*, **126**, e2021JC017858, <https://doi.org/10.1029/2021JC017858>.
- Gregory, J. M., and Coauthors, 2016: The Flux-Anomaly-Forced Model Intercomparison Project (FAFMIP) contribution to CMIP6: Investigation of sea-level and ocean climate change in response to CO₂ forcing. *Geosci. Model Dev.*, **9**, 3993–4017, <https://doi.org/10.5194/gmd-9-3993-2016>.
- , and Coauthors, 2019: Concepts and terminology for sea level: Mean, variability and change, both local and global. *Surv. Geophys.*, **40**, 1251–1289, <https://doi.org/10.1007/s10712-019-09525-z>.
- Griffies, S. M., and Coauthors, 2015: Impacts on ocean heat from transient mesoscale eddies in a hierarchy of climate models. *J. Climate*, **28**, 952–977, <https://doi.org/10.1175/JCLI-D-14-00353.1>.
- , and Coauthors, 2016: OMIP contribution to CMIP6: Experimental and diagnostic protocol for the physical component of the Ocean Model Intercomparison Project. *Geosci. Model Dev.*, **9**, 3231–3296, <https://doi.org/10.5194/gmd-9-3231-2016>.
- Gutjahr, O., D. Putrasahan, K. Lohmann, J. H. Jungclaus, J.-S. von Storch, N. Brüggemann, H. Haak, and A. Stössel, 2019: Max Planck Institute Earth System Model (MPI-ESM1.2) for the High-Resolution Model Intercomparison Project (High-ResMIP). *Geosci. Model Dev.*, **12**, 3241–3281, <https://doi.org/10.5194/gmd-12-3241-2019>.
- Haarsma, R. J., and Coauthors, 2016: High Resolution Model Intercomparison Project (HighResMIP v1.0) for CMIP6. *Geosci. Model Dev.*, **9**, 4185–4208, <https://doi.org/10.5194/gmd-9-4185-2016>.

- Häkkinen, S., and P. B. Rhines, 2004: Decline of subpolar North Atlantic circulation during the 1990s. *Science*, **304**, 555–559, <https://doi.org/10.1126/science.1094917>.
- , and —, 2009: Shifting surface currents in the northern North Atlantic Ocean. *J. Geophys. Res.*, **114**, C04005, <https://doi.org/10.1029/2008JC004883>.
- , —, and D. L. Worthen, 2011: Atmospheric blocking and Atlantic multidecadal ocean variability. *Science*, **334**, 655–659, <https://doi.org/10.1126/science.1205683>.
- Hallberg, R., and A. Gnanadesikan, 2006: The role of eddies in determining the structure and response of the wind-driven Southern Hemisphere overturning: Results from the Modeling Eddies in the Southern Ocean (MESO) project. *J. Phys. Oceanogr.*, **36**, 2232–2252, <https://doi.org/10.1175/JPO2980.1>.
- Hátún, H., A. B. Sandø, H. Drange, B. Hansen, and H. Valdimarsson, 2005: Influence of the Atlantic subpolar gyre on the thermohaline circulation. *Science*, **309**, 1841–1844, <https://doi.org/10.1126/science.1114777>.
- Hautala, S. L., D. H. Roemmich, and W. J. Schmitz Jr., 1994: Is the North Pacific in Sverdrup balance along 24°N? *J. Geophys. Res.*, **99**, 16 041–16 052, <https://doi.org/10.1029/94JC01084>.
- Hewitt, H. T., and Coauthors, 2017: Will high-resolution global ocean models benefit coupled predictions on short-range to climate timescales? *Ocean Modell.*, **120**, 120–136, <https://doi.org/10.1016/j.ocemod.2017.11.002>.
- , and Coauthors, 2020: Resolving and parameterising the ocean mesoscale in Earth system models. *Curr. Climate Change Rep.*, **6**, 137–152, <https://doi.org/10.1007/s40641-020-00164-w>.
- Hobday, A. J., and G. T. Pecl, 2014: Identification of global marine hotspots: Sentinels for change and vanguards for adaptation action. *Rev. Fish Biol. Fish.*, **24**, 415–425, <https://doi.org/10.1007/s11160-013-9326-6>.
- Hu, A., G. A. Meehl, W. Han, and J. Yin, 2011: Effect of the potential melting of the Greenland Ice Sheet on the meridional overturning circulation and global climate in the future. *Deep-Sea Res. II*, **58**, 1914–1926, <https://doi.org/10.1016/j.dsr2.2010.10.069>.
- Hurlburt, H. E., A. J. Wallcraft, W. J. Schmitz Jr., P. J. Hogan, and E. J. Metzger, 1996: Dynamics of the Kuroshio/Oyashio current system using eddy-resolving models of the North Pacific Ocean. *J. Geophys. Res.*, **101**, 941–976, <https://doi.org/10.1029/95JC01674>.
- Jungclaus, J. H., and Coauthors, 2013: Characteristics of the ocean simulations in the Max Planck Institute Ocean Model (MPIOM) the ocean component of the MPI-Earth system model. *J. Adv. Model. Earth Syst.*, **5**, 422–446, <https://doi.org/10.1002/jame.20023>.
- Karsten, R., H. Jones, and J. Marshall, 2002: The role of eddy transfer in setting the stratification and transport of a circumpolar current. *J. Phys. Oceanogr.*, **32**, 39–54, [https://doi.org/10.1175/1520-0485\(2002\)032<0039:TROETI>2.0.CO;2](https://doi.org/10.1175/1520-0485(2002)032<0039:TROETI>2.0.CO;2).
- Keil, P., T. Mauritsen, J. Jungclaus, C. Hedemann, D. Olonscheck, and R. Ghosh, 2020: Multiple drivers of the North Atlantic warming hole. *Nat. Climate Change*, **10**, 667–671, <https://doi.org/10.1038/s41558-020-0819-8>.
- Köhl, A., and D. Stammer, 2008: Decadal sea level changes in the 50-year GECCO ocean synthesis. *J. Climate*, **21**, 1876–1890, <https://doi.org/10.1175/2007JCLI2081.1>.
- Lee, T., S. Häkkinen, K. Kelly, B. Qiu, H. Bonekamp, and E. J. Lindstrom, 2010: Satellite observations of ocean circulation changes associated with climate variability. *Oceanography*, **23** (4), 70–81, <https://doi.org/10.5670/oceanog.2010.06>.
- Levermann, A., A. Griesel, M. Hofmann, M. Montoya, and S. Rahmstorf, 2005: Dynamic sea level changes following changes in the thermohaline circulation. *Climate Dyn.*, **24**, 347–354, <https://doi.org/10.1007/s00382-004-0505-y>.
- Li, D., and Coauthors, 2022: The impact of horizontal resolution on projected sea-level rise along US east continental shelf with the Community Earth System Model. *J. Adv. Model. Earth Syst.*, **14**, e2021MS002868, <https://doi.org/10.1029/2021MS002868>.
- Li, H., and J. S. von Storch, 2013: On the fluctuations of buoyancy fluxes simulated in a 1/10° OGCM. *J. Phys. Oceanogr.*, **43**, 1270–1287, <https://doi.org/10.1175/JPO-D-12-080.1>.
- Lyu, K., X. Zhang, and J. A. Church, 2020: Regional dynamic sea level simulated in the CMIP5 and CMIP6 models: Mean biases, future projections, and their linkages. *J. Climate*, **33**, 6377–6398, <https://doi.org/10.1175/JCLI-D-19-1029.1>.
- Magnan, A. K., and Coauthors, 2022: Sea level rise risks and societal adaptation benefits in low-lying coastal areas. *Sci. Rep.*, **12**, 10677, <https://doi.org/10.1038/s41598-022-14303-w>.
- Mauritsen, T., and Coauthors, 2019: Developments in the MPI-M Earth System Model version 1.2 (MPI-ESM1.2) and its response to increasing CO₂. *J. Adv. Model. Earth Syst.*, **11**, 998–1038, <https://doi.org/10.1029/2018MS001400>.
- Menary, M. B., and R. A. Wood, 2018: An anatomy of the projected North Atlantic warming hole in CMIP5 models. *Climate Dyn.*, **50**, 3063–3080, <https://doi.org/10.1007/s00382-017-3793-8>.
- Meredith, M. P., and A. M. Hogg, 2006: Circumpolar response of Southern Ocean eddy activity to a change in the Southern Annular Mode. *Geophys. Res. Lett.*, **33**, L16608, <https://doi.org/10.1029/2006GL026499>.
- Merrifield, M. A., 2011: A shift in western tropical Pacific sea level trends during the 1990s. *J. Climate*, **24**, 4126–4138, <https://doi.org/10.1175/2011JCLI3932.1>.
- Morris, M., D. Roemmich, and B. Cornuelle, 1996: Observations of variability in the South Pacific subtropical gyre. *J. Phys. Oceanogr.*, **26**, 2359–2380, [https://doi.org/10.1175/1520-0485\(1996\)026<2359:OOVITS>2.0.CO;2](https://doi.org/10.1175/1520-0485(1996)026<2359:OOVITS>2.0.CO;2).
- Morrow, R., G. Valladeau, and J.-B. Sallee, 2008: Observed subsurface signature of Southern Ocean sea level rise. *Prog. Oceanogr.*, **77**, 351–366, <https://doi.org/10.1016/j.pocean.2007.03.002>.
- Müller, W. A., and Coauthors, 2018: A higher-resolution version of the Max Planck Institute Earth System Model (MPI-ESM1.2-HR). *J. Adv. Model. Earth Syst.*, **10**, 1383–1413, <https://doi.org/10.1029/2017MS001217>.
- Nishikawa, H., S. Nishikawa, H. Ishizaki, T. Wakamatsu, and Y. Ishikawa, 2020: Detection of the Oyashio and Kuroshio fronts under the projected climate change in the 21st century. *Prog. Earth Planet. Sci.*, **7**, 29, <https://doi.org/10.1186/s40645-020-00342-2>.
- O'Neill, B. C., and Coauthors, 2017: The roads ahead: Narratives for shared socioeconomic pathways describing world futures in the 21st century. *Global Environ. Change*, **42**, 169–180, <https://doi.org/10.1016/j.gloenvcha.2015.01.004>.
- Pardaens, A. K., J. M. Gregory, and J. A. Lowe, 2011: A model study of factors influencing projected changes in regional sea level over the twenty-first century. *Climate Dyn.*, **36**, 2015–2033, <https://doi.org/10.1007/s00382-009-0738-x>.
- Prandi, P., M. Ablain, A. Cazenave, and N. Picot, 2012: A new estimation of mean sea level in the Arctic Ocean from satellite altimetry. *Mar. Geod.*, **35**, 61–81, <https://doi.org/10.1080/01490419.2012.718222>.

- Putrasahan, D. A., K. Lohmann, J.-S. von Storch, J. H. Jungclaus, O. Gutjahr, and H. Haak, 2019: Surface flux drivers for the slowdown of the Atlantic meridional overturning circulation in a high-resolution global coupled climate model. *J. Adv. Model. Earth Syst.*, **11**, 1349–1363, <https://doi.org/10.1029/2018MS001447>.
- , O. Gutjahr, H. Haak, J. H. Jungclaus, K. Lohmann, M. J. Roberts, and J. S. von Storch, 2021: Effect of resolving ocean eddies on the transient response of global mean surface temperature to abrupt 4xCO₂ forcing. *Geophys. Res. Lett.*, **48**, e2020GL09204, <https://doi.org/10.1029/2020GL092049>.
- Rahmstorf, S., J. E. Box, G. Feulner, M. E. Mann, A. Robinson, S. Rutherford, and E. J. Schaffernicht, 2015: Exceptional twentieth-century slowdown in Atlantic Ocean overturning circulation. *Nat. Climate Change*, **5**, 475–480, <https://doi.org/10.1038/nclimate2554>.
- Roberts, M. J., and Coauthors, 2018: The benefits of global high resolution for climate simulation: Process understanding and the enabling of stakeholder decisions at the regional scale. *Bull. Amer. Meteor. Soc.*, **99**, 2341–2359, <https://doi.org/10.1175/BAMS-D-15-00320.1>.
- Roemmich, D., J. Gilson, R. Davis, P. Sutton, S. Wijffels, and S. Riser, 2007: Decadal spinup of the South Pacific subtropical gyre. *J. Phys. Oceanogr.*, **37**, 162–173, <https://doi.org/10.1175/JPO3004.1>.
- , —, P. Sutton, and N. Zilberman, 2016: Multidecadal change of the South Pacific gyre circulation. *J. Phys. Oceanogr.*, **46**, 1871–1883, <https://doi.org/10.1175/JPO-D-15-0237.1>.
- Rose, S. K., O. B. Andersen, M. Passaro, C. A. Ludwigsen, and C. Schwatke, 2019: Arctic Ocean sea level record from the complete radar altimetry era: 1991–2018. *Remote Sens.*, **11**, 1672, <https://doi.org/10.3390/rs11141672>.
- Sakamoto, T. T., H. Hasumi, M. Ishii, S. Emori, T. Suzuki, T. Nishimura, and A. Sumi, 2005: Responses of the Kuroshio and the Kuroshio Extension to global warming in a high-resolution climate model. *Geophys. Res. Lett.*, **32**, L14617, <https://doi.org/10.1029/2005GL023384>.
- Semmler, T., J. Jungclaus, C. Danek, H. F. Goessling, N. V. Koldunov, T. Rackow, and D. Sidorenko, 2021: Ocean model formulation influences transient climate response. *J. Geophys. Res. Oceans*, **126**, e2021JC017633, <https://doi.org/10.1029/2021JC017633>.
- Shi, J.-R., L. D. Talley, S.-P. Xie, Q. Peng, and W. Liu, 2021: Ocean warming and accelerating Southern Ocean zonal flow. *Nat. Climate Change*, **11**, 1090–1097, <https://doi.org/10.1038/s41558-021-01212-5>.
- Small, R. J., and Coauthors, 2014: A new synoptic scale resolving global climate simulation using the Community Earth System Model. *J. Adv. Model. Earth Syst.*, **6**, 1065–1094, <https://doi.org/10.1002/2014MS000363>.
- Sonnwald, M., C. Wunsch, and P. Heimbach, 2019: Unsupervised learning reveals geography of global ocean dynamical regions. *Earth Space Sci.*, **6**, 784–794, <https://doi.org/10.1029/2018EA000519>.
- Stammer, D., 1997: Steric and wind-induced changes in TOPEX/Poseidon large-scale sea surface topography observations. *J. Geophys. Res.*, **102**, 20987–21009, <https://doi.org/10.1029/97JC01475>.
- , A. Cazenave, R. M. Ponte, and M. E. Tamisiea, 2013: Causes for contemporary regional sea level changes. *Annu. Rev. Mar. Sci.*, **5**, 21–46, <https://doi.org/10.1146/annurev-marine-121211-172406>.
- Stevens, B., and Coauthors, 2013: Atmospheric component of the MPI-M Earth System Model: ECHAM6. *J. Adv. Model. Earth Syst.*, **5**, 146–172, <https://doi.org/10.1002/jame.20015>.
- Straub, D. N., 1993: On the transport and angular momentum balance of channel models of the Antarctic Circumpolar Current. *J. Phys. Oceanogr.*, **23**, 776–782, [https://doi.org/10.1175/1520-0485\(1993\)023<0776:OTTAAM>2.0.CO;2](https://doi.org/10.1175/1520-0485(1993)023<0776:OTTAAM>2.0.CO;2).
- Sueyoshi, M., and T. Yasuda, 2012: Inter-model variability of projected sea level changes in the western North Pacific in CMIP3 coupled climate models. *J. Oceanogr.*, **68**, 533–543, <https://doi.org/10.1007/s10872-012-0117-9>.
- Suzuki, T., and H. Tatebe, 2020: Future dynamic sea level change in the western subtropical North Pacific associated with ocean heat uptake and heat redistribution by ocean circulation under global warming. *Prog. Earth Planet. Sci.*, **7**, 67, <https://doi.org/10.1186/s40645-020-00381-9>.
- Sverdrup, H. U., 1947: Wind-driven currents in a baroclinic ocean; with application to the equatorial currents of the eastern Pacific. *Proc. Natl. Acad. Sci. USA*, **33**, 318–326, <https://doi.org/10.1073/pnas.33.11.318>.
- Swart, N. C., S. T. Gille, J. C. Fyfe, and N. P. Gillett, 2018: Recent Southern Ocean warming and freshening driven by greenhouse gas emissions and ozone depletion. *Nat. Geosci.*, **11**, 836–841, <https://doi.org/10.1038/s41561-018-0226-1>.
- Terada, M., and S. Minobe, 2018: Projected sea level rise, gyre circulation and water mass formation in the western North Pacific: CMIP5 inter-model analysis. *Climate Dyn.*, **50**, 4767–4782, <https://doi.org/10.1007/s00382-017-3902-8>.
- NCL, 2019: The NCAR Command Language, version 6.6.2. UCAR/NCAR/CISL/TDD, <https://doi.org/10.5065/D6WD3XH5>.
- Thomas, M. D., A. M. De Boer, H. L. Johnson, and D. P. Stevens, 2014: Spatial and temporal scales of Sverdrup balance. *J. Phys. Oceanogr.*, **44**, 2644–2660, <https://doi.org/10.1175/JPO-D-13-0192.1>.
- Thompson, D. W. J., and S. Solomon, 2002: Interpretation of recent Southern Hemisphere climate change. *Science*, **296**, 895–899, <https://doi.org/10.1126/science.1069270>.
- van Westen, R. M., and H. A. Dijkstra, 2021: Ocean eddies strongly affect global mean sea-level projections. *Sci. Adv.*, **7**, eabf1674, <https://doi.org/10.1126/sciadv.abf1674>.
- , and Coauthors, 2020: Ocean model resolution dependence of Caribbean sea-level projections. *Sci. Rep.*, **10**, 14599, <https://doi.org/10.1038/s41598-020-71563-0>.
- von Storch, H., and F. W. Zwiers, 2002: *Statistical Analysis in Climate Research*. Cambridge University Press, 495 pp.
- Willebrand, J., S. G. H. Philander, and R. C. Pacanowski, 1980: The oceanic response to large-scale atmospheric disturbances. *J. Phys. Oceanogr.*, **10**, 411–429, [https://doi.org/10.1175/1520-0485\(1980\)010<0411:TORTLS>2.0.CO;2](https://doi.org/10.1175/1520-0485(1980)010<0411:TORTLS>2.0.CO;2).
- Wu, L., and Coauthors, 2012: Enhanced warming over the global subtropical western boundary currents. *Nat. Climate Change*, **2**, 161–166, <https://doi.org/10.1038/nclimate1353>.
- Wunsch, C., 2011: The decadal mean ocean circulation and Sverdrup balance. *J. Mar. Res.*, **69**, 417–434, <https://doi.org/10.1357/002224011798765303>.
- , and D. Roemmich, 1985: Is the North Atlantic in Sverdrup balance? *J. Phys. Oceanogr.*, **15**, 1876–1880, [https://doi.org/10.1175/1520-0485\(1985\)015<1876:ITNAIS>2.0.CO;2](https://doi.org/10.1175/1520-0485(1985)015<1876:ITNAIS>2.0.CO;2).
- Xiao, K., M. Chen, Q. Wang, X. Wang, and W. Zhang, 2020: Low-frequency sea level variability and impact of recent sea ice decline on the sea level trend in the Arctic Ocean from a high-resolution simulation. *Ocean Dyn.*, **70**, 787–802, <https://doi.org/10.1007/s10236-020-01373-5>.
- Yang, H., G. Lohmann, W. Wei, M. Dima, M. Ionita, and J. Liu, 2016: Intensification and poleward shift of subtropical western

- boundary currents in a warming climate. *J. Geophys. Res. Oceans*, **121**, 4928–4945, <https://doi.org/10.1002/2015JC011513>.
- , and Coauthors, 2020: Poleward shift of the major ocean gyres detected in a warming climate. *Geophys. Res. Lett.*, **47**, e2019GL085868, <https://doi.org/10.1029/2019GL085868>.
- Yeager, S., 2015: Topographic coupling of the Atlantic overturning and gyre circulations. *J. Phys. Oceanogr.*, **45**, 1258–1284, <https://doi.org/10.1175/JPO-D-14-0100.1>.
- Yin, J., 2012: Century to multi-century sea level rise projections from CMIP5 models. *Geophys. Res. Lett.*, **39**, L17709, <https://doi.org/10.1029/2012GL052947>.
- , M. E. Schlesinger, and R. J. Stouffer, 2009: Model projections of rapid sea-level rise on the northeast coast of the United States. *Nat. Geosci.*, **2**, 262–266, <https://doi.org/10.1038/ngeo462>.
- , S. M. Griffies, and R. J. Stouffer, 2010: Spatial variability of sea level rise in twenty-first century projections. *J. Climate*, **23**, 4585–4607, <https://doi.org/10.1175/2010JCLI3533.1>.
- Zhang, X., J. A. Church, S. M. Platten, and D. Monselesan, 2014: Projection of subtropical gyre circulation and associated sea level changes in the Pacific based on CMIP3 climate models. *Climate Dyn.*, **43**, 131–144, <https://doi.org/10.1007/s00382-013-1902-x>.